

This discussion paper is/has been under review for the journal Atmospheric Chemistry and Physics (ACP). Please refer to the corresponding final paper in ACP if available.

Development and impact of hooks of high droplet concentration

R. C. George et al.

Development and impact of hooks of large droplet concentration on remote southeast Pacific stratocumulus

R. C. George, R. Wood, C. S. Bretherton, and G. Painter

University of Washington, Seattle, Washington, USA

Received: 19 December 2012 – Accepted: 19 January 2013 – Published: 24 January 2013

Correspondence to: R. C. George (rheag@uw.edu)

Published by Copernicus Publications on behalf of the European Geosciences Union.

Title Page

Abstract

Introduction

Conclusions

References

Tables

Figures

⏪

⏩

◀

▶

Back

Close

Full Screen / Esc

Printer-friendly Version

Interactive Discussion

Abstract

Over the southeastern Pacific (SEP), droplet concentration (N_d) in the typically unpolluted marine stratocumulus west of 80° W (> 1000 km offshore) is periodically strongly enhanced in zonally-elongated “hook”-shaped arcs that increase albedo. Here, we examine three hook events using the chemistry version of the Weather Research and Forecasting model (WRF-Chem) with 14 km horizontal resolution, satellite data and aircraft data from the VAMOS Ocean-Cloud-Atmosphere-Land Study Regional Experiment (VOCALS-REx). A particularly strong hook yields insights to the development, decay, and radiative impact of these features. Hook development occurs with N_d increasing to polluted levels over the remote ocean primarily due to entrainment of cloud condensation nuclei (CCN) from the free troposphere (FT). The feature advects north-westward until the FT CCN source is depleted, after which N_d decreases over a few days due to precipitation and dilution. The model suggests that the FT CCN source supplying the hook consists of high concentrations of small accumulation mode aerosols that contribute a relatively small amount of aerosol mass to the MBL. The aerosol particles originate mainly from a pulse of offshore flow that transports Santiago region ($33\text{--}35^\circ$ S) emissions to the marine FT.

To provide a sustained hook CCN source, the FT transport of pollution plumes to the remote ocean requires strong, deep offshore flow. Such flow is favored by a trough approaching the South American coast and a southeastward shift of the climatological subtropical high pressure system. The model simulations show precipitation suppression in the hook and a corresponding increase in liquid water path (LWP) compared with a simulation without anthropogenic sources. LWP also increases in time as the hook evolves due to increasing stability and decreasing subsidence. WRF-Chem suggests that DMS significantly influences the aerosol number and size distributions in a hook, but that hooks do not form without FT CCN. The Twomey effect contributes $\sim 50\text{--}70\%$ of the albedo increase due the presence of the hook, while secondary aerosol indirect effects and meteorological influences also contribute significantly.

Development and impact of hooks of high droplet concentration

R. C. George et al.

Title Page

Abstract

Introduction

Conclusions

References

Tables

Figures



Back

Close

Full Screen / Esc

Printer-friendly Version

Interactive Discussion



Development and impact of hooks of high droplet concentration

R. C. George et al.

Title Page

Abstract

Introduction

Conclusions

References

Tables

Figures

⏪

⏩

◀

▶

Back

Close

Full Screen / Esc

Printer-friendly Version

Interactive Discussion

The source of hook aerosols is difficult to determine with the available observations alone. The model explains the observations and puts them in context of the factors influencing hook formation. Two other weaker hooks during VOCALS-REx are not as well simulated but are also associated with FT offshore flow near Santiago. Hooks demonstrate the importance of free-tropospheric transport of aerosols in modulating the droplet concentration in the southeastern Pacific stratocumulus deck, and present a formidable challenge to simulate accurately in large scale models.

1 Introduction

The transport of anthropogenic aerosol and precursors from continents to remote marine regions impacts cloud microphysical and radiative properties (e.g. Schwartz et al., 2002). Aerosol number concentration, size distribution, chemical composition (which influences hygroscopicity), mixing state and environmental properties (such as relative humidity, vertical velocity, and supersaturation) determine how many aerosols activate as cloud droplets (Penner et al., 2001). Aerosols affect cloud microphysical properties (e.g. droplet number concentration, N_d), and indirectly their radiative and macrophysical properties (liquid water path, LWP, and cloud fraction, CF). The first aerosol indirect effect (AIE), or the Twomey effect (Twomey, 1974), describes the increase in cloud albedo due to increasing N_d and droplet surface area absent changes in cloud macrophysics. Secondary AIEs involving changes to cloud macrophysical properties can enhance or offset the first AIE (Ackerman et al., 2004; Lohmann and Feichter, 2005; Bretherton et al., 2007; Wood, 2007). Together, AIEs are the primary sources of uncertainty in the anthropogenic impact on the global radiative budget (Randall et al., 2007).

Anthropogenic aerosols and their gaseous precursors emitted from urban sources along the Chilean coastline advect over the stratocumulus-dominated southeast Pacific (SEP; $\sim 10\text{--}40^\circ\text{S}$, $70\text{--}90^\circ\text{W}$, Huneus et al., 2006; Allen et al., 2011). The microphysics of marine stratocumulus are susceptible to aerosols (Platnick and Twomey,

1994) and the clouds over the SEP forming in extremely clean air from the remote southern Pacific are particularly susceptible to aerosol increases. Mean low-level southeasterly flow induced by the subtropical high (on average centered near 30° S, 90° W) encourages lower tropospheric transport of continental air over the SEP. Further, the Andes form a high barrier within 200 km of the coast that discourages eastward transport of Chilean emissions. The SEP is therefore a region of strong contrasts between clean and polluted airmasses and an excellent testbed for studying cloud-aerosol interactions. The Andes interact with synoptic scale dynamics (through mechanisms such as diurnal pumping), leading to episodic outflow of continental boundary layer air into the marine free troposphere (FT; Rahn and Garreaud, 2010b; Allen et al., 2011; Toniazzo et al., 2011). Due to subsidence associated with the subtropical high (Klein and Hartmann, 1993) and increasing marine boundary layer (MBL) depth with distance from the coast (Bretherton et al., 2010), this continental air can be transported by winds moving to the northwest and may eventually intersect the marine inversion and be entrained into the MBL (Allen et al., 2011).

Precursor gaseous species can affect aerosols through in-cloud processing, contribute to new aerosol formation through nucleation, or condense onto pre-existing particles (Seinfeld and Pandis, 1998). Chilean anthropogenic emissions of sulfate, organic and other primary and secondary aerosols as well as their gaseous precursors (such as SO₂ which oxidizes to sulfate) originate mainly from industrial and urban sources, including copper mining and the Santiago metropolis (Tsapakis et al., 2002; Schüller et al., 2008). Santiago's emissions combined with topographic transport restrictions causes this city to have one of the largest mass loadings of PM₁₀ (aerosols smaller than 10 μm) in the world (> 50 μg m⁻³ in 2006, Muñoz and Alcañiz, 2012). Thus, the dynamic conditions that allow air from this region to advect over the SEP may lead to strong AIEs.

Over the SEP, *N_o* estimates derived from MODIS satellite retrievals (George and Wood, 2010) show strong mean zonal gradients from the relatively "pristine" MBL west of 80° W to high concentrations near to the Chilean coast (Fig. 1a). The increase east

Development and impact of hooks of high droplet concentration

R. C. George et al.

Title Page

Abstract

Introduction

Conclusions

References

Tables

Figures



Back

Close

Full Screen / Esc

Printer-friendly Version

Interactive Discussion



of 75° W is associated with anthropogenic aerosols transported by two pathways: direct advection in the MBL from coastal sources; episodic transport in the FT and entrainment into the MBL (Huneeus et al., 2006; Allen et al., 2011).

Composites of MODIS N_d and derived reflected solar flux at the top of the atmosphere are constructed for those days when mean N_d in the domain 19–21° S, 82–86° W is more than 87 cm⁻³ (one standard deviation above the climatological mean). This box is chosen to sample the region where N_d contributes most to albedo variance (see Fig. 5 in George and Wood, 2010). Comparing these increased offshore N_d composites (Fig. 1b) with the mean state (Fig. 1a) reveals a shift in the pattern of N_d not only within the compositing box (which, by construction must occur) but over a broad region between the box and the coast. The hook-like shape of enhanced N_d extends southeastward from the compositing domain (Fig. 1b) and strongly enhances the albedo and the Twomey effect offshore (Fig. 1c vs. d). Around the compositing box, days with high N_d experience 25–40 W m⁻² larger reflected solar flux than on average and 10–20 W m⁻² (~ 40–50%) of this is due to the Twomey effect. The remote composites therefore demonstrate important microphysically-driven albedo variability in an often pristine region. The non-Twomey component of the albedo increases may be caused by secondary AIE's and/or meteorological covariability with N_d . This motivates our need to investigate the reasons for strong N_d variability over the remote SEP.

Instantaneous images over consecutive days showing N_d from the GOES satellite (Sect. 2.1) during periods of elevated offshore N_d typically show a narrow band of high N_d characterized by an east-west “hook” of high N_d with maximum N_d in the range 150–350 cm⁻³ standing out against marine background values of ~ 50 cm⁻³. The example in Fig. 2 (17–20 October 2008) occurred during the VAMOS Ocean-Cloud-Atmosphere-Land Study Regional Experiment (VOCALS-REx; Wood et al., 2011b) that took place 15 October–16 November 2008. During REX, hooks that extended west of 80° W coincided with research flights at least 3 times (18 October, 2 November and 15 November), and we refer to these cases as Hooks 1, 2, and 3, respectively.

Development and impact of hooks of high droplet concentration

R. C. George et al.

Title Page

Abstract

Introduction

Conclusions

References

Tables

Figures



Back

Close

Full Screen / Esc

Printer-friendly Version

Interactive Discussion

Development and impact of hooks of high droplet concentration

R. C. George et al.

Title Page

Abstract

Introduction

Conclusions

References

Tables

Figures

⏪

⏩

◀

▶

Back

Close

Full Screen / Esc

Printer-friendly Version

Interactive Discussion



Laboratory (<http://www-angler.larc.nasa.gov/>) to compute N_d at 4 km horizontal resolution, 30 min time resolution by the method of Bennartz (2007) with a corrected formulation for the vertical condensation rate (from Albrecht et al., 1990). While the N_d accuracy depends upon solar zenith angle, midday retrievals reasonably match VO-CALS flight observations and MODIS estimates (Painemal et al., 2012).

European Centre for Medium Range Weather Forecasting (ECMWF) operational analyses on a $0.125 \times 0.125^\circ$ grid with 91 hybrid model levels at 6 h time resolution are used to drive 3-D and 2-D trajectories (see Appendix) presented here. 2-D isobaric trajectories at a mid-MBL pressure of 950 hPa track satellite cloud features advecting with the MBL flow quite well, lending confidence in the use of trajectory analysis. We attribute the agreement to the high quality of the ECMWF wind analysis (Bretherton et al., 2010) and the relatively weak vertical shear of winds within the MBL.

2.2 Hook1 observations

Of the three cases, Hook1 has the strongest anomalous N_d and extends the furthest west into the remote ocean, and is particularly striking on 19 October at 15:00 UTC (Fig. 2c). Isobaric two-dimensional forward and backward trajectories at 950 hPa based on ECMWF analyses initialized from points on the hook on 19 October at 15:00 UTC trace the hook advection quite well between 18–20 October (Fig. 2b–d). However, prior to this on 17 October (Fig. 2a) the three outermost trajectory points have $N_d < 70 \text{ cm}^{-3}$, typical of pristine marine air, and all trajectory points have significantly lower N_d than on 19 October. Although accumulated trajectory errors could potentially contribute to this, it appears that the hook in N_d is not explained solely by advection of an aerosol-rich air mass from the coast within the MBL.

Entrainment of FT aerosols thus warrants investigation as a significant contributing hook source. Three-dimensional back trajectories using ECMWF analyses (Fig. 3) from points along the hook (Fig. 2) at the level of the inversion (identified as the height of minimum temperature where relative humidity is larger than 50 % from ECMWF profiles, which is 1–1.5 km at most hook locations) on 18 October at 12:00 UTC indicate

subsidence and advection from the South American coast at 700–800 mb between 34–37° S (Fig. 3). This suggests that a possible source of hook aerosols could be entrainment of FT air that has been lofted by upslope flow in the vicinity of Central/Southern Chile. Although the two westernmost trajectories do not quite intersect the coast, the clearly connected nature of the observed hook (Fig. 2c) suggests that these outer hook locations have similar sources. All the FT trajectories may be subject to increasing errors near the coast and close to the Andes, where upslope flow is closely confined to the orography (e.g. Toniazzo et al., 2011). Despite not intersecting the coast, the westernmost 3-D trajectories get closer to it than do the corresponding 2-D MBL trajectories (from Fig. 2, also reproduced in Fig. 3), further supporting the idea that advection of continental aerosols to the remote ocean is more likely in the FT than the MBL.

The latitudes where most of the 3-D hook back trajectories approach the coast are mainly to the south of the major anthropogenic sources (including Santiago at 33.5° S, 70.7° W, 500 m a.m.s.l. and the Caletones copper smelter at 34.1° S, 70.5° W, 1700 m a.m.s.l., see Fig. 3). Over land the back trajectories do not appear to originate from this source region. The small point emissions near sea-level on the coast near 37° S are insufficient to provide significant hook CCN. Coastal biogenic, dust and fire related aerosols are unlikely to cause the heavily polluted N_d seen in the hook given they do not explain the large mean N_d nearer the coast (Allen et al., 2011). Volcanic emissions and copper smelters in Northern Chile (north of 30° S) are large sources of SO₂, but hook trajectories do not indicate obvious influence from this region.

The VOCALS C-130 flight that took place 18 October (Wood et al., 2011b) along 20° S and sampled the large remote N_d a few degrees north of the trajectory end points in Fig. 3 measured 100–200 cm⁻³ CCN concentration (at a supersaturation $\sigma = 0.4$ –0.5 %) during above-cloud flight legs, which is insufficient to explain the observed 150–300 cm⁻³ N_d measured during in-cloud legs and noted in satellite data. Given the lack of an observed FT source in this case, it is difficult with REx observations alone to establish the source of hook CCN.

Development and impact of hooks of high droplet concentration

R. C. George et al.

Title Page

Abstract

Introduction

Conclusions

References

Tables

Figures

⏪

⏩

◀

▶

Back

Close

Full Screen / Esc

Printer-friendly Version

Interactive Discussion



3 Model

We use a regional chemical transport model (WRF-Chem) to understand processes controlling the origins and development of the hook features and their impact on clouds. WRF-Chem simulates most of chemical, thermodynamic, and aerosol-related processes relevant in the SEP.

3.1 Model configuration

We run the WRF-Chem version 3.2 (Grell et al., 2005; Fast et al., 2006) over an outer domain spanning 0–50° S, 60–100° W at 0.5 × 0.5° horizontal resolution with 27 vertical levels, 10–12 of which are typically in the MBL, from 15 October to 16 November 2008 following nine days of spin-up. To accurately simulate the near-mountain flow and associated transport processes, we show results primarily from a nested, higher resolution domain spanning 3–40° S, 65–95° W, at 0.125 × 0.125° resolution. For the outer domain, NCEP 1 × 1° final analysis (FNL) winds, pressure, thermal and moisture fields at 6 hourly time resolution provide the meteorological boundary conditions. Chemical boundary and initial conditions come from the Model for Ozone and Related chemical Tracers (MOZART-4; Emmons et al., 2010). An inventory compiled for VOCALS-REX described by Mena-Carrasco et al. (2010) provides point and area emissions from anthropogenic and volcanic sources. Lima (12° S, 77° W) emissions have been reduced by a factor of 100 because in the simulation they cause excessive column SO₂ at Lima that was not observed by the Ozone Monitoring Instrument in 2004–2005 (Carn et al., 2007) and excessively high N_q in the northern part of the domain not present in MODIS retrievals. These emissions do not affect hook formation in the model. No biogenic or fire emissions are included in the simulations. WRF-Chem's online wind-blown dust emissions are excluded from the simulations because they are much larger than MOZART-4 dust emissions in this region and in any case do not affect CCN concentrations. Sea spray emissions are computed following Gong et al. (1997), and do not

Development and impact of hooks of high droplet concentration

R. C. George et al.

Title Page

Abstract

Introduction

Conclusions

References

Tables

Figures



Back

Close

Full Screen / Esc

Printer-friendly Version

Interactive Discussion



include organic components, which are small during the VOCALS campaign (Shank et al., 2012).

The first and second aerosol indirect effects, as well as the direct and semi-direct effects are represented through interactions between aerosols, radiation, and clouds (Fast et al., 2006; Gustafson et al., 2007; Chapman et al., 2009). The Lin microphysics parameterization (Gustafson et al., 2007; Chapman et al., 2009) is used, and has been modified to include prognostic cloud droplet number. The RRTM longwave radiation scheme, the Goddard shortwave radiation (Chou et al., 1998), the Grell-3-D ensemble cumulus scheme, the Monin-Obukhov surface scheme, and the NOAH land surface model comprise other chosen options. Based on code from Xin-Zhong Liang at the University of Maryland we implement the University of Washington PBL scheme (UWPBL; Bretherton and Park, 2009) designed for the Community Atmosphere Model (CAM) to improve representation of stratocumulus in coarse resolution models.

Chemical reactions are represented via the Regional Acid Deposition Model version 2 (RADM2; Stockwell et al., 1990; Chang et al., 1990), which employs the Quasi-Steady State Approximation method for 38 predicted, 3 constant, and 22 diagnosed species. It includes aqueous phase chemistry (Fahey and Pandis, 2001) that is coupled to the microphysics and aerosol schemes. Because DMS is not included in this mechanism, we have added a uniform ocean surface DMS concentration of 2.8 nML^{-1} with a parameterized sea-air flux based on Nightingale et al. (2000) dependent on wind speed as described in the VOCA Modeling Experiment Specification¹, and we have added reactions of DMS with OH and NO_3 to form SO_2 . The MADE/SORGAM modal aerosol option (Ackermann et al., 1998; Schell et al., 2001) defines aerosol properties and behavior, and tracks three size modes representing the Aitken, accumulation and coarse modes of aerosols. Aerosol particles activate to cloud droplets using the parameterization of Abdul-Razzak and Ghan (2000), based on critical supersaturation and a Gaussian distribution of updraft speeds. The cloud droplet activation code was

¹Available at http://www.atmos.washington.edu/~mwyant/vocals/model/VOCA_Model.Spec.htm

Development and impact of hooks of high droplet concentration

R. C. George et al.

Title Page

Abstract

Introduction

Conclusions

References

Tables

Figures



Back

Close

Full Screen / Esc

Printer-friendly Version

Interactive Discussion



modified to use the UWPBL turbulent kinetic energy (TKE) output following Morrison and Pinto (2005) rather than the eddy diffusivity of heat to compute subgrid vertical velocity variance, as was done in CAM (Gettelman et al., 2010).

Three basic simulations are conducted in this study. The first simulation “Anth”, which we use as our baseline simulation, has all the aforementioned emissions. A second labeled “NoAnth” has no anthropogenic emissions and a third “NoDMS” has all emissions other than DMS. Additional simulations to explore the impact of removing emissions in specific locations are described in Sect. 4.6.

3.2 Model evaluation during REx

Other studies have used versions of WRF-Chem to simulate the VOCALS-REx period and have been able to reproduce, with some fidelity, the key cloud and chemical features, including 20° S time-mean longitudinal gradients of sulfate, aerosol concentration and N_d (Yang et al., 2011; Saide et al., 2012). Although our simulations employ slightly different parameterization options and resolution, it also reasonably reproduces REx mean conditions. The gradient of REx mean N_d along 20° S agrees well with satellite and aircraft data (Fig. 4) even though the magnitude is underestimated by 10–30%. Like the Yang et al. (2011) and Saide et al. (2012) simulations, the MBL aerosol and sulfate concentrations are biased low, but capture the longitudinal gradient. Unlike Saide et al. (2012) we do not tune the background SO_2 in the FT to match VOCALS observations, so mean SO_2 and CCN in the FT are also lower than observed. As in Saide et al. (2012), we find that Lin microphysics leads to a mean high precipitation bias along 20° S, which partly explains the model’s low LWP bias (Fig. 5), may explain the low bias in N_d and possibly shortens the lifetime of aerosol species in the MBL.

Development and impact of hooks of high droplet concentration

R. C. George et al.

Title Page

Abstract

Introduction

Conclusions

References

Tables

Figures

⏪

⏩

◀

▶

Back

Close

Full Screen / Esc

Printer-friendly Version

Interactive Discussion



4 Hook1

4.1 Modeled Hook1 evaluation

The model captures the life cycle of a hook between 17–20 October, shown in Fig. 6, that is in broad agreement with the observed Hook1 shown in Fig. 2, although there are some differences in its timing and extent. On 19 October at 15:15 UTC the observed N_d spatial pattern (Fig. 2c) is a clear example of what we define as a hook. At this time, there is a modeled hook (Fig. 6e), but it is shifted several degrees to the north of the observed hook. The modeled hook 24 h earlier (Fig. 6c) more accurately represents the observed hook at 15:00 UTC on 19 October, indicative of a timing bias. In addition, the westward tip of the modeled hook is about 5 degrees further west than the observed hook. The N_d maxima in the modeled hook are comparable to those in the observed hook, and the arched shape of the hook is well-captured, but the observed hook is considerably narrower than the modeled hook. The time evolution of N_d is in good agreement with observations, with both showing a persistent feature advecting northward through the region over several days before decaying.

On the other hand, several features of the pattern of observed and modeled N_d do not match. The model simulates a second large hook north of the one we have focused on (Fig. 6b, c). Although the observations do indicate a protuberance of polluted N_d reaching west of 80° W ahead of Hook1 (Fig. 2b, c), this observed feature is not so clearly hook-shaped, does not extend as far westward, and is more spatially separated from Hook1 than in the model (Figs. 2b and 6c). The model also does not reproduce the high N_d values east of 75° W between 18–26° S.

Model MBL 2-D trajectories accurately follow the modeled hook feature (Fig. 6). Trajectories are computed both forward and backward starting from points along the maximum model N_d on 19 October at 03:00 UTC to trace both the development and decay of the modeled hook. Trajectories are initialized two model levels below the inversion, between 910–950 hPa, and are computed with horizontal wind components only. Figure 6 suggests that the modeled hook along these trajectories coincides with a large

Development and impact of hooks of high droplet concentration

R. C. George et al.

Title Page

Abstract

Introduction

Conclusions

References

Tables

Figures



Back

Close

Full Screen / Esc

Printer-friendly Version

Interactive Discussion



source of CCN just above the inversion. Over time, this modeled FT source decreases in number concentration due to entrainment and falls behind the hook due to vertical wind shear.

Measured SO_2 and CCN concentration (at $\sigma = 0.4\text{--}0.5\%$) in the FT during the C-130 Hook1 flight (on 18 October) indicates the flight did not sample a strong FT aerosol source (Fig. 7) that can explain the coincident large N_d (e.g. Fig. 2b). The time offset between model and satellite observations of the peak hook N_d crossing 20°S is 24 h, so flight data is compared with model output 24 h earlier (Fig. 7), on 17 October. Although flight SO_2 values are in agreement with the branch of model SO_2 elevated above the background slightly south of the flight measurements, this is partly due the mean bias in the model FT SO_2 concentrations. The 40–50 pptv observed in the remote ocean FT is slightly larger than the 20–40 pptv observed on average by C-130 flights during REx along 20°S (Allen et al., 2011), but because the CCN measured in the FT is also not notably large this was not interpreted as a significant FT pollution event. The CCN flight measurements agree very well with the model (except in the furthest SW leg), which inspires some confidence in the model representation. The model suggests that a large FT CCN source coincided with Hook1 (Fig. 7b), but further south than the flight measured. Additionally this modeled FT CCN source contributes to the northern N_d hook that is erroneously large as explained above. It is likely that during the flight N_d was large due to a FT source that had already entrained. At the comparison time modeled N_d is not large in the flight region (Fig. 6a), but later times in the model (e.g. Fig. 6b) indicate that large N_d ahead of a large FT CCN source can occur and is modeled, just not in the same times and places as observed. The flight did not sample the hook edge, and thus likely simply did not sample a region of entrainment of high concentrations of FT CCN.

Development and impact of hooks of high droplet concentration

R. C. George et al.

Title Page

Abstract

Introduction

Conclusions

References

Tables

Figures

⏪

⏩

◀

▶

Back

Close

Full Screen / Esc

Printer-friendly Version

Interactive Discussion



4.2 Interpolation over 2-D trajectories

4.2.1 Hook development

Figure 8 shows cloud and aerosol properties interpolated along WRF-Chem 2-D MBL backward and forward trajectories initialized at a set of points along the hook at 03:00 UTC on 19 October (see Fig. 6), and demonstrates the development and decay of Hook1. We construct a time series of the average in-cloud N_d over all trajectories with LWP $> 0.01 \text{ g m}^{-2}$ (Fig. 8a). The concentration $N_{\text{CCN,FT}}$ of CCN in the model layer above the marine inversion peaks at $\sim 600 \text{ cm}^{-3}$, some 15 h before the peak of CCN within the MBL, and decreases rapidly thereafter. By the time of peak N_d , fewer than 100 cm^{-3} FT CCN remain. During the second half of the hook life cycle, the $N_{\text{CCN,FT}}$ decreases to low levels (Fig. 8a) and precipitation reaching the surface increases (not shown) while air entrained from the FT has low CCN concentrations, so $N_{\text{CCN,MBL}}$ and N_d decrease without a major source to replace droplets lost to precipitation and dilution. This provides strong evidence that entrainment of FT aerosol is a dominant source of simulated hook aerosol and N_d . The earlier increase of $N_{\text{CCN,FT}}$ (Fig. 8a) is due to the arrival at the inversion of a subsiding aerosol layer (see Sect. 4.4).

The peak in hook N_d lags the final rise in MBL CCN concentration ($N_{\text{CCN,MBL}}$) by ~ 9 h and the $N_{\text{CCN,FT}}$ peak by 24 h (Fig. 8a). The former lag is explained by a reduced supersaturation maximum and therefore a lower fraction of CCN activated in the clouds during daytime because TKE is stabilized by solar absorption (local transition from night to day occurs at $\sim 12:00$ UTC). This effect is also seen during the subsequent day starting at 12:00 UTC on 19 October. The daytime decline in TKE reduces the turbulent vertical velocity variance and thus maximum effective in-cloud supersaturation, which increases in the size of the smallest particle activated and decreases the fraction of aerosol particles that become droplets. The daytime separation between N_d and $N_{\text{CCN,MBL}}$ is indicative of a population of small CCN entrained from the FT that is strongly sensitive to the maximum supersaturation achieved during the activation

Development and impact of hooks of high droplet concentration

R. C. George et al.

[Title Page](#)[Abstract](#)[Introduction](#)[Conclusions](#)[References](#)[Tables](#)[Figures](#)[⏪](#)[⏩](#)[◀](#)[▶](#)[Back](#)[Close](#)[Full Screen / Esc](#)[Printer-friendly Version](#)[Interactive Discussion](#)

process. That is, there are small CCN that are not activated, but would in a more turbulent cloud with higher supersaturation.

The activation of these additional CCN occurs during the 6–9 h leading to peak N_d , which also corresponds to a peak in TKE. The increase in $N_{\text{CCN,MBL}}$ is the essential condition enabling hook formation, but MBL turbulence and chemistry also influences the variability in N_d over the lifecycle of a hook. As the hook feature forms, FT SO_2 is elevated well above MBL values, so entrainment is a source of SO_2 (Fig. 8b), which is oxidized to sulfate in the MBL. This entrainment source explains some, but not all, of the large increase in MBL SO_4 aerosol mass during the hook growth period. A surface sulfur source is also important as demonstrated by the fact that the MBL SO_4 mass is reduced by $\sim 40\%$ in the NoDMS simulation (Fig. 8b). Despite the importance of the surface DMS source for increasing MBL sulfate aerosol mass, $N_{\text{CCN,MBL}}$ is not strongly sensitive to the surface DMS source (Fig. 8a). This is primarily because the SO_2 mainly condenses onto and enlarges existing particles. While this does move some particles into the CCN size range, this is not a major effect, consistent with previous modeling studies (e.g. Woodhouse et al., 2010).

The value of N_d is more sensitive than is $N_{\text{CCN,MBL}}$ to the inclusion of DMS (Fig. 8a). This is also seen in Fig. 9a, b, which compares the N_d fields at one particular time for NoDMS with the control Anth simulation. This sensitivity is due to a complex consequence of several factors, including changes in particle size and TKE differences (Fig. 8a). However, another consideration is that in the NoDMS run, the hook in N_d is displaced a few degrees southeast, so the maximum N_d is not sampled by the trajectories shown in Fig. 8a.

Although the hook event appears to result from significant entrainment of CCN, the total accumulation mode aerosol mass per unit volume above the inversion is less than $0.5 \mu\text{g m}^{-3}$, much smaller than the $2\text{--}3 \mu\text{g m}^{-3}$ averaged in the MBL (Fig. 8e). The mean accumulation mode dry volume diameter (calculated from mass and number values) is only $\sim 0.04 \mu\text{m}$ in the FT vs $\sim 0.1 \mu\text{m}$ in MBL (Fig. 8f) during hook development. With sea salt aerosols comprising a large fraction of the accumulation mode aerosol mass in

Development and impact of hooks of high droplet concentration

R. C. George et al.

Title Page

Abstract

Introduction

Conclusions

References

Tables

Figures



Back

Close

Full Screen / Esc

Printer-friendly Version

Interactive Discussion

the MBL, only a small relative increase in MBL aerosol mass occurs as the FT aerosols are entrained. Thus the FT source is comprised of numerous small aerosols, strongly impacts the MBL aerosol number concentrations and has little impact on aerosol mass within the hook. It is also worth noting that the contribution of organic aerosols to the overall aerosol mass in the FT immediately above the hook is only 10–20% in the model, and so most of the contribution to CCN associated with the hook is from sulfate.

4.2.2 Hook impacts on cloud properties

Without anthropogenic aerosols (in the NoAnth simulation), no hook forms (Fig. 9). Thus, comparing the cloud properties in the NoAnth and Anth simulations at the same locations/times allows us to distinguish cloud macrophysical changes due to anthropogenic aerosols from meteorological changes. Their differences between the NoAnth and Anth simulations maximize near peak hook N_d (\sim 03:00 UTC on 19 October, Fig. 8a) and show diurnal modulation. The hook aerosols cause increased TKE (Fig. 8a) and LWP (Fig. 8d), most likely due to the suppression of precipitation due to increased CCN (Fig. 8c) and associated reduction in stabilization (Ackerman et al., 2004). The precipitation below cloud base is $1\text{--}2\text{ mm day}^{-1}$ in the NoAnth simulation right around the time of the peak hook N_d , and is cut by roughly 50% due to the hook aerosols. A strong diurnal cycle in LWP is found in both the Anth and NoAnth cases (Fig. 8d) but hook aerosols increase LWP more at night (especially during the night of the peak hook N_d). This is likely a consequence of the strong coincident precipitation suppression. We examine the impacts of these cloud macrophysical changes on the albedo in Sect. 4.3. From 00:00–09:00 UTC on 20 October surface precipitation is suppressed (not shown), but sub-cloud base precipitation rate is only weakly suppressed and Anth LWP is much smaller than the night before, due to a weakened influence of hook aerosols and dips strongly at 09:00 UTC. This doesn't coincide with a more rapid CCN loss rate, so may indicate a process that reduces droplet size during hook decay.

For context, Fig. 8d also shows the mean LWP from the Anth simulation at the same times of day/locations from the entire REx period. Other than exhibiting a strong diurnal

Development and impact of hooks of high droplet concentration

R. C. George et al.

Title Page

Abstract

Introduction

Conclusions

References

Tables

Figures



Back

Close

Full Screen / Esc

Printer-friendly Version

Interactive Discussion



cycle, the REx mean LWP does not change markedly following the northward motion of the evolving trajectory position, indicating that the LWP evolution along the trajectory in the Anth and NoAnth runs is not driven by geographical variation in meteorology. That the nighttime LWP increases from the night of the 17–18 October to the following night in the NoAnth simulation means some of the increase in Anth simulation nighttime LWP is caused by meteorological peculiarities of the hook event. During the initial hook formation stages subsidence is stronger than average (Fig. 10), which causes lower inversion heights than average (not shown) despite weaker lower tropospheric stability than in the REx mean. Following the developing hook the stability increases, which maintains the strong capping inversion and weakens entrainment, which suppresses the lifting of the cloud base level. The weakening subsidence allows the MBL top to rise despite the strengthening stability, so cloud thickness and LWP increase.

4.3 Impact of hook on albedo

LWP and N_d (discussed above) and CF (not shown) are, on average over the hook, greater due to the hook-forming aerosols in the Anth simulation than in the NoAnth simulation (Fig. 8), so the secondary indirect effects of anthropogenic emissions generally enhance the Twomey effect on hook albedo. We estimate model albedo using model-derived N_d , LWP and CF following the method of George and Wood (2010). This allows us to separate the Twomey effect, the impacts of microphysics (N_d), from albedo changes due to secondary effects (LWP and CF). These computed albedo values are about 10 % larger than albedo derived from model top of atmosphere short-wave flux due to the influence of atmosphere above the clouds not addressed by the computation and differences in scattering assumptions between the albedo computation and the model. For each day following the hook the daily solar insolation weighted mean albedo is computed to capture the net hook AIE impact. The albedo from the Anth simulation along the hook trajectory is 35–50 % larger than in the NoAnth simulation (Fig. 11). Albedo computed using the Anth simulation macrophysical properties, but NoAnth values of N_d (blue circles in Fig. 11) demonstrates that the Twomey effect

Development and impact of hooks of high droplet concentration

R. C. George et al.

Title Page

Abstract

Introduction

Conclusions

References

Tables

Figures



Back

Close

Full Screen / Esc

Printer-friendly Version

Interactive Discussion



contributes ~50–70% of the hook albedo enhancement over that in NoAnth, while aerosol-induced LWP and CF changes and meteorological variability between Anth and NoAnth simulations contribute the rest. Note that Fig. 11's representation of the Twomey effect uses the Anth simulation as the reference case, which is different from studies using global climate models which would typically use NoAnth as the reference. The ~20% temporal increase in Anth albedo following the hook (from 0.41 to 0.49) demonstrates the significant change in albedo that an individual hook events can cause. The smaller (~13%; 0.3 to 0.34) temporal increase in NoAnth albedo is due partly to the increase in LWP associated with the increasing stability and weakening subsidence. Removing DMS from the simulation causes a 20–25% reduction in hook albedo, and indicates a systematic effect of aerosol growth due to DMS-derived SO₂ (Fig. 11). Before the hook has formed on 17 October, excluding DMS reduces albedo to a magnitude similar to the NoAnth simulation and a ~43% temporal increase in the NoDMS hook albedo indicates omitting this important SO₂ source would cause an overestimation in the albedo change caused by the hook. DMS thus impacts the background MBL properties that noticeably affect the entrained hook aerosols and resulting radiative changes.

4.4 3-D pathway of hook FT aerosol

The evolution of aerosol and cloud properties along 2-D MBL trajectories allows us to examine how the hook is formed by entrainment of FT aerosols, but this cannot identify the original source of the aerosols, nor does it explain the meteorological conditions that allow for the transport of pollution to the remote ocean. Model 3-D back trajectories (not shown) from regions of large FT CCN indicate that the Santiago region (33–35° S, 70–72° W) is the dominant source of aerosols and precursors for the hook. It is more illustrative to examine forward 3-D trajectories initialized among the Santiago-region sources that eventually transport offshore and contribute to the hook CCN. The circle markers in Fig. 12 show one such representative trajectory. It begins 15 October at 18:00 UTC at 2 km altitude near the surface above the Caletones smelter

Development and impact of hooks of high droplet concentration

R. C. George et al.

Title Page

Abstract

Introduction

Conclusions

References

Tables

Figures



Back

Close

Full Screen / Esc

Printer-friendly Version

Interactive Discussion



Development and impact of hooks of high droplet concentration

R. C. George et al.

Title Page

Abstract

Introduction

Conclusions

References

Tables

Figures

⏪

⏩

◀

▶

Back

Close

Full Screen / Esc

Printer-friendly Version

Interactive Discussion



(34.125° S 70.5° W, 1700 m a.m.s.l.). The Caletones smelter contributes SO₂ emissions of 108 kTon yr⁻¹, or ~ 40 % of the total SO₂ emissions south of 28° S and west of the Andes. Although smelters alone make a relatively small contribution to the mean SEP aerosol population (Twohy et al., 2012), this trajectory represents one pathway in which copper smelter emissions may reach the remote ocean. The left panels of Figs. 13 and 14 show longitude-height slices at key times at the latitude of the trajectory location; the right panels show corresponding RE_x-mean conditions. The trajectory is situated within a plume of high CCN concentrations (cyan contours) and SO₂ concentrations (yellow contours) and reaches the inversion level near 80.5° W, 20.5° S on 18 October at 15:00 UTC (Fig. 14c), contributing aerosols to MBL in the Hook1 growth phase (see Fig. 8).

During the early days of this trajectory (15–16 October), anomalously strong southward Andes barrier winds (Rahn and Garreaud, 2010a; Toniazzo et al., 2011) prevail north of 37° S over the Andes (compare left and right panels, Fig. 13a–d), causing stronger than average southward transport of Santiago region emissions. This is supported by an upper level trough (Fig. 15b) ahead of a southeastward shifting subtropical high and cyclonic flow ahead of this feature near Santiago. The polluted air advects southward along and up the Andes and reaches 37–40° S, a typically clean region with few local pollution sources (Fig. 13f), on 16 October. During this period of southward transport, ascent over the Andes is also stronger than average (Fig. 13a vs. 13b). Some of the vertical enhancement may be due to the normal diurnal cycle, as in the vicinity of the Andes the mountain breeze maximum and land-sea circulation are associated with ascent later in the day (Toniazzo et al., 2011). At the trajectory start time (local time ~ 3 p.m.) ascent is therefore expected. However, there is also stronger than average onshore flow aloft (due to the anomalous cyclonic flow) encountering the Andes barrier (Fig. 13a, b) and enhancing the vertical motion. The upward motion leads to a large plume of SO₂ and CCN rising to over 5 km near 36° S nine hours after the trajectory start (Fig. 13c). The trajectory actually moves over the crest of the Andes. At this time,

the flow at 3–6 km contains little or no zonal component as the trajectory nears the center of the mid-tropospheric cyclone (Fig. 15b).

The shift of the subtropical high towards the coast on 16 October drives strong surface southerlies at 36° S and the approaching upper level trough encourages onshore flow at 700 hPa to the north of 36° S and offshore flow to the south (Fig. 15b). Normally, the flow near and south of Santiago is onshore throughout the lower troposphere (Fig. 13b, d, f) and does not therefore carry urban emissions over the remote ocean. On average surface emissions in the Santiago area advect weakly northward (similar latitude shown in Fig. 13b), but if lofted high enough (> 2 km) to reach the Andes northerly barrier flow, the primary direction of transport is southward. In the Hook1 case, the pollution plume, having moved southward to 39° S, is then subject to offshore flow over a deep layer from the surface to over 6 km (Fig. 13e). This day coincides with the peak in the strength of the subtropical high (Fig. 15b), which is shifted southeast of its REX mean (Fig. 15d). The lower height of the Andes at 39° S compared with Santiago's latitude also reduces their blocking effect and allows westward flow at lower levels and a deep column of offshore aerosol transport.

Southward transport of Santiago region emissions occurs regularly and is visible in the modeled REX-mean SO₂ concentrations. For example, at 36° S SO₂ concentrations exceeding 100 pptv extend above 4 km on average (Fig. 13d). Usually, this plume is advected eastward across the Andes; it is the enhancement of this feature (over 500 pptv above 4 km, Fig. 13c) due to the strengthened southward winds, combined with meteorological conditions conducive to subsequent offshore flow that allows for the formation of the modeled Hook1. Nucleation of the enhanced SO₂ in this specific case is also important to create the high CCN seen in Hook1, but not in the mean state.

By 06:00 UTC on 17 October (Fig. 14a) northwestward flow has looped the trajectory back to its starting latitude, but west of its starting point, by which time the subtropical high has partly relaxed towards its climatological mean (Fig. 15c). As the upper level trough nears the coast it suppresses the normal zonal flow and induces a strong northward flow, especially at 74–75° W (Fig. 12). Together with stronger than average

Development and impact of hooks of high droplet concentration

R. C. George et al.

Title Page

Abstract

Introduction

Conclusions

References

Tables

Figures

⏪

⏩

◀

▶

Back

Close

Full Screen / Esc

Printer-friendly Version

Interactive Discussion

subsidence west of the trough on 17 October, between 06:00 and 21:00 UTC on 17 October (Fig. 14a, b), the trajectory advects westward by only about 1° , but northward by about $7\text{--}8^\circ$ and subsides by about 1.5 km. The top of the plume also drops substantially, and for the remainder of the FT plume lifespan it subsides and spreads above the inversion level. By the time the trajectory reaches 20.5° S on 15:00 UTC 18 October the plume is entraining into the MBL and its vertical extent reaches only to 1 km above the inversion (Fig. 14c).

Whether a particular polluted plume in the FT contributes to a hook downstream is dependent on the timing, magnitude and location of offshore flow and its altitude above the stratocumulus. For example, at 36° S on 03:00 UTC 16 October (Fig. 13c), a plume of SO_2 between $1\text{--}3$ km ($72\text{--}75^\circ$ W) extends offshore in low level easterlies. But as it advects northwards (not shown) it encounters onshore flow associated with near-coast low pressure (Fig. 15c) and never contributes to remote CCN. The broad polluted plume already existing in the FT at 34° S $75\text{--}81^\circ$ W at the start of the shown trajectory (Fig. 13a) advects northward until around 28° S (not shown), at which point westward flow associated with the subtropical high transports the plume out over the ocean, providing the source aerosol for the modeled hook to the north of (i.e. preceding) Hook1 (Fig. 6b). As mentioned in Sect. 4.1, this feature doesn't match satellite observations well but may represent a noted protuberance of high N_d ahead of Hook1. Back trajectories indicate this modeled plume advected offshore near 39° S on 14 October, and before that had traveled southward from the Santiago region, similar to the transport mechanism associated with Hook1. This offshore flow is associated with the same approaching ridge/trough that affects Hook1, and a strong surface coastal low on 13 October.

Figure 12 shows two additional 3-D trajectories, initialized in a similar elevated SO_2 plume presumably due to earlier southward transport. Despite the difference in starting locations, all three trajectories advect offshore at a similar time, but at different pressures (from 570 hPa to 680 hPa). The lower two trajectories follow very similar paths. The highest trajectory ultimately contributes to the hook further west and later than the

Development and impact of hooks of high droplet concentration

R. C. George et al.

Title Page

Abstract

Introduction

Conclusions

References

Tables

Figures

⏪

⏩

◀

▶

Back

Close

Full Screen / Esc

Printer-friendly Version

Interactive Discussion

Development and impact of hooks of high droplet concentration

R. C. George et al.

Title Page

Abstract

Introduction

Conclusions

References

Tables

Figures

⏪

⏩

◀

▶

Back

Close

Full Screen / Esc

Printer-friendly Version

Interactive Discussion



lower two as it takes longer to subside. However, the faster speed at which this trajectory travels is offset by the weakened influence of subtropical high induced easterly flow at these higher altitudes, increasing the distance it must travel to the remote ocean compared to the lower trajectories. Thus in this case transport of high CCN into the remote ocean depends on offshore flow at a level that is high enough to avoid intersecting the MBL before reaching the remote ocean, but low enough to be turned westward by the low level flow between 20–30° S.

The model 3-D trajectory traced in Figs. 13 and 14 advects from land to ocean at a pressure level near 610 hPa, which is somewhat higher by ~ 100 hPa than those of the ECMWF 3-D back trajectories starting at the inversion above the hook (Fig. 3). In the model, large SO₂ and CCN concentrations extend up to ~ 500 hPa (Fig. 13c) and the hook of elevated N_d extends further west than the observed hook. This is consistent with the model simulating overly strong upward vertical transport over land, leading to CCN in the FT in the model that extends further north and west than the observed N_d suggests.

4.5 Interpolation over 3-D trajectories

Most chemical and aerosol fields interpolated over the 3-D trajectory described in Sect. 4.4 do not vary much during marine FT transport (not shown). However, Aitken mode number concentrations decline from ~ 800 cm⁻³ to ~ 400 cm⁻³ over 12 h during the early part of the descent toward the MBL top while there is minimal change in the accumulation mode concentration, suggesting coagulation of the relatively large number concentrations of the small ~ 0.01 μm particles in the plume. Following this period, accumulation mode, Aitken mode, and CCN number concentrations remain steady until very near the inversion level. Additionally the SO₂ concentration remains steady, as does sulfate mixing ratio, though once the trajectory is near the MBL SO₄ gradually increases by 40 % due to aqueous phase processing of entrained and DMS-derived SO₂. This indicates relatively simple advection without significant chemical/aerosol changes until entry into clouds. There is no evidence of strong nucleation events, significant

aerosol size changes, or any other mechanism that would change the CCN as a plume of polluted air transports over the marine SEP in the FT.

4.6 Sources of hook aerosols

Neither DMS-derived SO_4 nor long-range transport of species input via boundary conditions, both of which are present in the NoAnth simulation, cause hook formation (Fig. 9d). A model run without DMS (NoDMS) has lower N_d by $\sim 15\%$ both in and outside the hook, but the NoDMS hook N_d peak occurs about 1–2 degrees “behind”, or southeast of, the Anth simulation hook (Fig. 9a, b). In the NoDMS run, both Aitken and accumulation mode number concentrations are very close to those in the Anth simulation, but the accumulation mode particles are smaller, which shifts the MBL size distribution and reduces the number of particles activated. A binned aerosol scheme would probably be more appropriate than a modal scheme to investigate this further.

When emissions south of 31°S are excluded, no clear Hook1 forms (not shown). Emissions from the Northern Chilean smelters and volcanoes do not appear to advect to the remote SEP (Twohy et al., 2012). In a simulation without anthropogenic emissions east of the Andes (70°W) south of 30°S (Fig. 9c), the hook is also shifted behind the Anth hook with smaller peak N_d magnitude, but the basic hook characteristics remain intact. The emissions east of the Andes are small compared to the Santiago region, but also advect offshore with the cyclonic flow and affect the hook shape, extent and magnitude. These sensitivity studies clearly demonstrate that transport of anthropogenic aerosol sources from the Santiago region is the dominant source of Hook1 N_d , but the location and magnitude of the hook is sensitive to processes affecting the FT plume and the MBL CCN.

Development and impact of hooks of high droplet concentration

R. C. George et al.

Title Page

Abstract

Introduction

Conclusions

References

Tables

Figures



Back

Close

Full Screen / Esc

Printer-friendly Version

Interactive Discussion



5 Other hooks

Our analysis shows that are four key elements of the Hook1 event are (a) Santiago area emissions; (b) an initial southward and upward transport; (c) subsequent offshore flow; (d) subsidence and entrainment. Two other pronounced hooks formed during REx.

In this section we present observations and simulations of these cases, looking for these same elements. Unfortunately, WRF-Chem underestimates the offshore extent and magnitude of the observed N_d maximum in Hook3 and especially Hook2 (Fig. 16). However, in both of these cases, the model does simulate offshore flow of Santiago region emissions in the FT that subsides, entrains and enhances N_d west of the region most impacted by coastal aerosols on average (Fig. 1).

5.1 Hook 2: 2 November 2008

Hook2, at its peak, is an extended region of high N_d cloud reaching from the Chilean coast between 24–30° S in a northwestward direction out to 20° S, 83° W on 2 November (Fig. 16a). ECMWF MBL 2-D back trajectories from the offshore tip of the hook trace a region of high N_d clouds to near the coast (not shown), indicating that some pollution transport takes place within the MBL from coastal sources to the remote ocean, in contrast to Hook1. The transition from the polluted hook to the clean conditions was sampled near 22° S, 80° W between 09:00 and 12:00 UTC on 2 November by the VOCALS C130 flight RF08. Near the coast CCN concentrations exceeding 500 cm⁻³ (at $\sigma = 0.5\%$) were measured in the FT along 20° S, but much lower concentrations (~ 150–180 cm⁻³) further west along 20° S indicate a lack of FT aerosol support for the polluted tongue.

WRF-Chem severely underestimates the hook N_d for this event (Fig. 16c) although a region of somewhat increased N_d extends from the Santiago region to ~ 25° S, 75° W. This region does not develop further over the remote ocean at later model times. This suggests the model is not correctly simulating the offshore advection of aerosol. There is offshore flow of FT air with 200 cm⁻³ CCN on 30–31 October (Fig. 16b) extending

Development and impact of hooks of high droplet concentration

R. C. George et al.

Title Page

Abstract

Introduction

Conclusions

References

Tables

Figures



Back

Close

Full Screen / Esc

Printer-friendly Version

Interactive Discussion



from south of Santiago. On the day of the hook, FT SO₂ concentrations reach 400 pptv along the western edge of the modeled region of elevated N_d region, but no substantial model FT source of CCN remains over the ocean (Fig. 16c). The simulated region of large FT SO₂ does not reach west of 77° W or north of 25° S, consistent with the RF08 observations of a relatively unpolluted FT further to the northwest.

Figure 17 shows 3-D WRF-Chem back-trajectories from the FT above the modeled region of elevated N_d seen in Fig. 16c. They indicate lofted air from south of Santiago subsiding towards the MBL (Fig. 17a). That higher concentrations of FT SO₂ but smaller number concentrations of CCN are transported offshore in the FT than in the Hook1 case indicates weaker nucleation processes prior to offshore advection and reduces the impact of the entrained plume on N_d (because entrained SO₂ is more likely to add mass to existing aerosols rather than nucleate more particles in the MBL). Three possible reasons why WRF-Chem does not produce the distinct observed hook are (1) excessive CCN loss rates within the MBL, which quickly remove CCN advected in the MBL from coastal pollution sources; (2) underestimated nucleation of new particles in the pollution plume that can subsequently serve as CCN, which may prevent the FT aerosol plume from maintaining the offshore portion of the hook; (3) modeling errors in the altitude, latitude, and/or magnitude of offshore flow of polluted air necessary for continental air to reach the remote ocean.

Like Hook1, a southeastward shifted subtropical high behind an upper level trough both precede the observed hook, but the sea level pressure anomaly is much weaker than in Hook 1 and the upper level trough intersects the coastline further north. This causes a weaker event and a different hook shape, but nonetheless favors transport of pollution into the remote ocean.

5.2 Hook 3: 15 November 2008

Hook3, like Hook1, extends far offshore (Fig. 16d), as seen in the satellite retrieval chosen to overlap with VOCALS flight RF14 that sampled the hook out to 80° W near 20° S on 15 November between 15:00 and 20:00 UTC. A layer with mean SO₂ concentrations

Development and impact of hooks of high droplet concentration

R. C. George et al.

Title Page

Abstract

Introduction

Conclusions

References

Tables

Figures



Back

Close

Full Screen / Esc

Printer-friendly Version

Interactive Discussion



of 550 ppt was observed in the FT less than 100 m above cloud top at 80° W, 20–22° S. The mean concentration of CCN at $\sigma = 0.5\%$ during this flight leg was 1100 cm^{-3} indicating an unusually polluted FT over the remote SEP.

The model produces a hook qualitatively similar to, but less extensive than that observed (Fig. 16f). It captures a hook of large FT CCN concentrations (Fig. 16f), but the CCN concentration at 80° W is much smaller than measured. Again, model back trajectories indicate that much of the FT transport is composed of Santiago region emissions (Fig. 17b). However, Fig. 17b also shows that some model 3-D back trajectories from the hook correspond to offshore flow at 27–28° S in the FT, so sources north of Santiago may also contribute to the polluted air over the remote ocean. From both sources, high concentrations of SO₂ and CCN advect upward and southward, then offshore, but less far south than in Hook1. 2-D MBL model back trajectories encounter the coast just to the south of the Santiago region, so MBL transport cannot be ruled out as a hook source of CCN in this case. However, over the four days of transport from the coast to the remote ocean, aerosol number loss processes such as precipitation and cloud processing reduce the likelihood of it being the sole source of hook CCN.

As with the other hook cases, a high pressure system shifted southward and eastward from its climatological mean occurs. The high stays close the coast south of Santiago for several days, contributing to Hook3 and, subsequently, a much stronger hook on 19 November. The upper level flow is not characterized by the same system noted in Hook1 and Hook2, but a near-shore trough does allow for upper level offshore flow. Polluted FT plumes contributing to Hook3 travel north of 24° S before westward advection past 75° W (Fig. 17b), far enough away from the southward shifted subtropical high to experience weaker subsidence than average. Thus, FT polluted layers that have not yet been entrained into the MBL are observed on RF14 lying above the remote ocean cloud. In the model a plume of high CCN concentration at 2 km altitude at 28° S, 72.5° W on 06:00 UTC 14 November does not intersect the MBL until it reaches 22° S, 82° W on 15 November at 12:00 UTC. This took 12 h longer to subside to the inversion and traveled about 3.5 degrees longitude further than the Hook1 trajectory (cf.

Development and impact of hooks of high droplet concentration

R. C. George et al.

Title Page

Abstract

Introduction

Conclusions

References

Tables

Figures



Back

Close

Full Screen / Esc

Printer-friendly Version

Interactive Discussion

Fig. 14b, c) subsidence from near 2 km to the inversion (over a similar latitude change). This weaker subsidence allows for greater westward FT transport than other situations of offshore flow at 2 km. Nevertheless, Hook1 extends further west than Hook3 in the model because of the deeper layer of FT offshore transport.

5.3 Commonalities between Hooks

Although the model does not reproduce all three major observed N_d hooks in the REx period well, it does simulate FT offshore flow of polluted plumes of CCN/SO₂ from the Santiago region and as far south as 35.5° S in the model. The model does not simulate FT offshore flow this far south at any time during REx besides the 2–3 days preceding the three hook cases. Hence, it suggests that FT flow off the Chilean coast near or just south of Santiago is an important component of hook formation during REx. Emissions at other latitudes and altitudes may contribute to the observed hook in some cases, but Santiago region emissions are key. Santiago-area pollution plumes experience some lofting (to altitudes of 3–6 km) and southward transport in all three cases, especially Hook1, before being advected offshore, after which they subside and are entrained into the MBL, contributing to the hook feature in N_d . All three hooks also have evidence of MBL transport of regions of elevated N_d after the FT source has been depleted. Although in some cases direct MBL transport from coastal regions may substantially contribute to hook CCN (especially Hook2), entrainment appears key to supporting offshore high N_d . In summary, remote ocean N_d hooks appear strongly linked to FT transport of Santiago region emissions, though more cases would need to be studied to gain absolute confidence in this association.

6 Conclusions

Periodic free-tropospheric transport of anthropogenic emissions to the typically stratocumulus-dominated pristine SEP remote ocean produces strong AIEs and a large

Development and impact of hooks of high droplet concentration

R. C. George et al.

Title Page

Abstract

Introduction

Conclusions

References

Tables

Figures

⏪

⏩

◀

▶

Back

Close

Full Screen / Esc

Printer-friendly Version

Interactive Discussion



differences in the wind field and vertical mixing, especially on the slopes of the Andes, the assumed emissions, and both the free-tropospheric and boundary layer processing of aerosol.

The first hook event experiences a significant increase in N_d over the remote ocean that cannot be explained by MBL advection and model results indicate entrainment of FT aerosols is responsible. Albedo at the peak of the hook is larger than a simulation without anthropogenic aerosols, which is due largely to the Twomey effect though secondary AIEs enhance this the Twomey effect and contribute 30–50 % of the net albedo change. Albedo also increases during hook development primarily due to aerosol changes, but an increase in stability and weakening subsidence associated with the coincident meteorology is also noted in the simulation without anthropogenic aerosols and explains part of the albedo change.

Synoptic meteorological conditions and their interactions with the Andes topography are important to the FT CCN transport that leads to hook formation. Subsidence and the increase in MBL depth offshore often limit the westward reach of anthropogenic aerosols in the FT, so high concentrations of CCN in the remote FT must originate from significant lofting up the Andes prior to offshore flow or weak subsidence during offshore transport. However, the required westward flow is associated with the north end of the subtropical high and does not extend to heights of more than 5–6 km at most. Other meteorological scenarios may lead to offshore transport, but the ones during REx all coincided with a southeastward shift of the subtropical high associated with an upper-tropospheric trough approaching the Chilean coast from the west, causing changes to the normal direction of transport (Rahn and Garreaud, 2010a). Whether the transport is in the FT or the MBL, hook events require meteorologically anomalous offshore flow driven by changes in the strength and location of the subtropical high and a method to preserve or even enhance high CCN concentrations in the MBL during passage to the remote region.

Although there is general agreement between the observations and model for strong hook events, the model fails to match exactly the timing and extent of any of the hook

Development and impact of hooks of high droplet concentration

R. C. George et al.

Title Page

Abstract

Introduction

Conclusions

References

Tables

Figures

⏪

⏩

◀

▶

Back

Close

Full Screen / Esc

Printer-friendly Version

Interactive Discussion

features studied here. Because they affect the variability of N_d and therefore AIEs over the remote ocean and are so difficult to reproduce with a model, hooks represent a significant challenge in quantifying regional AIEs. The difficulty simulating them, even with a regional model with relatively high resolution, reflects the very precise sequence of meteorological conditions must occur for these narrow bands of elevated offshore transport to bring aerosols to the right place at the right time. In addition, to capture the impact of a hook on radiation the model must accurately represent the aerosol processing within the MBL that adds aerosol mass from DMS-produced SO_2 , in addition to turbulent and activation processes within stratocumulus. Correctly capturing and quantifying the variability in AIEs thus represents a formidable challenge.

Appendix A

Trajectories

A Trajectories are computed by solving the equation

$$d\mathbf{X}/dt = \mathbf{v}(\mathbf{X}(t), t) \quad (\text{A1})$$

where t is time, \mathbf{X} is the position vector, and \mathbf{v} the wind vector in 3 dimensions. This equation is integrated over time using the iterative Petterssen (1940) scheme.

$$\mathbf{X}(t_i) = \mathbf{X}(t_{j-1}) + dt/2 \cdot \{\mathbf{v}(\mathbf{X}(t_{j-1}), t_{j-1}) + \mathbf{v}(\mathbf{X}(t_i), t_i)\} \quad (\text{A2})$$

$\mathbf{X}_{\text{init}}(t_i)$ is initially approximated as $\mathbf{X}(t_{j-1}) + \mathbf{v}(\mathbf{X}(t_{j-1}), t_{j-1}) \cdot dt$. Then $\mathbf{v}(\mathbf{X}_{\text{init}}(t_i), t_i)$ is interpolated to compute a new $\mathbf{X}(t_i)$ from Eq. (A2). If $\mathbf{X}(t_i) - \mathbf{X}_{\text{init}}(t_i)$ is below a threshold error, the iteration stops, otherwise $\mathbf{X}(t_i)$ becomes the new $\mathbf{X}_{\text{init}}(t_i)$ and the calculation continues until $\mathbf{X}(t_i) - \mathbf{X}_{\text{init}}(t_i)$ is sufficiently small. 3-D ECMWF trajectories are computed using its hybrid sigma pressure coordinates, while the WRF-Chem trajectories are based on the terrain following eta coordinate. 2-D trajectories are computed by

Development and impact of hooks of high droplet concentration

R. C. George et al.

Title Page

Abstract

Introduction

Conclusions

References

Tables

Figures

⏪

⏩

◀

▶

Back

Close

Full Screen / Esc

Printer-friendly Version

Interactive Discussion



setting vertical velocity to 0. Trajectories are computed both forward and backward in time.

2-D MBL model trajectories start from two model levels below the inversion, which is around 900–950 mb and 2-D ECMWF trajectories start at 950 mb. Trajectories remain at a fixed eta or hybrid sigma pressure level, and given the deepening of the boundary layer in the SEP east-west direction, trajectories forward in time are further below the inversion than earlier along the trajectory. Due to the relative homogeneity (little shear) of winds within the boundary layer, these trajectories track the hook (model or observed) well.

Over the ocean computed trajectories are assumed to capture the direction and magnitude of transport because of the strong meteorological forcing of the subtropical high and relative homogeneity of the MBL winds. Near the Andes the land-sea thermal contrast, diurnal land heating cycle, and mountain effects complicate the wind fields. Enough variability occurs within the 6 h timesteps of the ECMWF that confidence in the path of the ECMWF trajectories over land is greatly reduced. Model trajectories computed at 3 h intervals are subject to similar time resolution errors, but in some cases follow plumes of high CCN quite well (Figs. 13 and 14).

Over short periods of time an idealize parcel will be representative of air motion (Stohl et al., 1995). The length of time that trajectories continue to represent bulk transport of air is a limiting factor in using trajectory analysis. Sources of trajectory errors include the length of the timestep, wind field errors due to subgrid variability not captured by interpolation, and wind gradient errors (Riddle et al., 2006).

Acknowledgements. The authors thank David Covert, Daniel Grosvenor, and Joel Thornton for discussions and guidance. MODIS data were obtained from the NASA Goddard Land Processes data archive. The authors also thank Patrick Minnis and his research group for making GOES-derived cloud properties available. NCEP reanalysis data were obtained from NCEP Climate Diagnostics Center. VOCALS flight data were provided by NCAR/EOL under sponsorship of the National Science Foundation. <http://data.eol.ucar.edu/>.

Development and impact of hooks of high droplet concentration

R. C. George et al.

Title Page

Abstract

Introduction

Conclusions

References

Tables

Figures



Back

Close

Full Screen / Esc

Printer-friendly Version

Interactive Discussion



References

- Abdul-Razzak, H. and Ghan, S. J.: A parameterization of aerosol activation 2. Multiple aerosol types, *J. Geophys. Res.-Atmos.*, 105, 6837–6844, 2000. 2502
- Ackerman, A. S., Kirkpatrick, M. P., Stevens, D. E., and Toon, O. B.: The impact of humidity above stratiform clouds on indirect aerosol climate forcing, *Nature*, 432, 1014–1017, doi:10.1038/nature03174, 2004. 2495
- Ackermann, I. J., Hass, H., Memmesheimer, M., Ebel, A., Binkowski, F. S., and Shankar, U.: Modal aerosol dynamics model for Europe: development and first applications, *Atmos. Environ.*, 32, 2981–2999, doi:10.1016/S1352-2310(98)00006-5, 1998. 2502
- Albrecht, B. A., Fairall, C. W., Thomson, D. W., White, A. B., Snider, J. B., and Schubert, W. H.: Surface based remote sensing of the observed and the Adiabatic liquid water content of stratocumulus clouds, *Geophys. Res. Lett.*, 17, 89–92, doi:10.1029/GL017i001p00089, 1990. 2499
- Allen, G., Coe, H., Clarke, A., Bretherton, C., Wood, R., Abel, S. J., Barrett, P., Brown, P., George, R., Freitag, S., McNaughton, C., Howell, S., Shank, L., Kapustin, V., Brekhovskikh, V., Kleinman, L., Lee, Y.-N., Springston, S., Toniazzo, T., Krejci, R., Fochesatto, J., Shaw, G., Krecl, P., Brooks, B., McMeeking, G., Bower, K. N., Williams, P. I., Crosier, J., Crawford, I., Connolly, P., Allan, J. D., Covert, D., Bandy, A. R., Russell, L. M., Trembath, J., Bart, M., McQuaid, J. B., Wang, J., and Chand, D.: South East Pacific atmospheric composition and variability sampled along 20° S during VOCALS-REx, *Atmos. Chem. Phys.*, 11, 5237–5262, doi:10.5194/acp-11-5237-2011, 2011. 2495, 2496, 2497, 2498, 2505, 2520
- Bandy, A. R., Thornton, D. C., Tu, F. H., Blomquist, B. W., Nadler, W., Mitchell, G. M., and Lenschow, D. H.: Determination of the vertical flux of dimethyl sulfide by eddy correlation and atmospheric pressure ionization mass spectrometry (APIMS), *J. Geophys. Res.-Atmos.*, 107, 4743, doi:10.1029/2002JD002472, 2002. 2498
- Bennartz, R.: Global assessment of marine boundary layer cloud droplet number concentration from satellite, *J. Geophys. Res.-Atmos.*, 112, D02201, doi:10.1029/2006JD007547, 2007. 2499
- Bretherton, C. S. and Park, S.: A new moist turbulence parameterization in the community atmosphere model, *J. Climate*, 22, 3422–3448, doi:10.1175/2008JCLI2556.1, 2009. 2502

Development and impact of hooks of high droplet concentration

R. C. George et al.

Title Page

Abstract

Introduction

Conclusions

References

Tables

Figures

⏪

⏩

◀

▶

Back

Close

Full Screen / Esc

Printer-friendly Version

Interactive Discussion



Development and impact of hooks of high droplet concentration

R. C. George et al.

Title Page

Abstract

Introduction

Conclusions

References

Tables

Figures

⏪

⏩

◀

▶

Back

Close

Full Screen / Esc

Printer-friendly Version

Interactive Discussion



- Bretherton, C. S., Blossey, P. N., and Uchida, J.: Cloud droplet sedimentation, entrainment efficiency, and subtropical stratocumulus albedo, *Geophys. Res. Lett.*, 34, L03813, doi:10.1029/2006GL027648, 2007. 2495
- Bretherton, C. S., Wood, R., George, R. C., Leon, D., Allen, G., and Zheng, X.: Southeast Pacific stratocumulus clouds, precipitation and boundary layer structure sampled along 20° S during VOCALS-REx, *Atmos. Chem. Phys.*, 10, 10639–10654, doi:10.5194/acp-10-10639-2010, 2010. 2496, 2499
- Carn, S. A., Krueger, A. J., Krotkov, N. A., Yang, K., and Levelt, P. F.: Sulfur dioxide emissions from Peruvian copper smelters detected by the ozone monitoring instrument, *Geophys. Res. Lett.*, 34, L09801, doi:10.1029/2006GL029020, 2007. 2501
- Chang, J. S., Binkowski, F., Seaman, N., McHenry, J., Samson, P., Stockwell, W., Walcek, C., Madronich, S., Middleton, P., Pleim, J., and Lansford, H.: The regional acid deposition model and engineering model, in: *Acidic Deposition: State of Science and Technology*, National Acid Precipitation Assessment Program, Washington DC., 25–78, 1990. 2502
- Chapman, E. G., Gustafson Jr., W. I., Easter, R. C., Barnard, J. C., Ghan, S. J., Pekour, M. S., and Fast, J. D.: Coupling aerosol-cloud-radiative processes in the WRF-Chem model: Investigating the radiative impact of elevated point sources, *Atmos. Chem. Phys.*, 9, 945–964, doi:10.5194/acp-9-945-2009, 2009. 2502
- Chou, M. D., Suarez, M. J., Ho, C. H., Yan, M. M. H., and Lee, K. T.: Parameterizations for cloud overlapping and shortwave single-scattering properties for use in general circulation and cloud ensemble models, *J. Climate*, 11, 202–214, doi:10.1175/1520-0442(1998)011<0202:PFCOAS>2.0.CO;2, 1998. 2502
- Emmons, L. K., Walters, S., Hess, P. G., Lamarque, J.-F., Pfister, G. G., Fillmore, D., Granier, C., Guenther, A., Kinnison, D., Laepple, T., Orlando, J., Tie, X., Tyndall, G., Wiedinmyer, C., Baughcum, S. L., and Kloster, S.: Description and evaluation of the Model for Ozone and Related chemical Tracers, version 4 (MOZART-4), *Geosci. Model Dev.*, 3, 43–67, doi:10.5194/gmd-3-43-2010, 2010. 2501
- Fahey, K. M. and Pandis, S. N.: Optimizing model performance: variable size resolution in cloud chemistry modeling, *Atmos. Environ.*, 35, 4471–4478, doi:10.1016/S1352-2310(01)00224-2, 2001. 2502
- Fast, J. D., Gustafson Jr., W. I., Easter, R. C., Zaveri, R. A., Barnard, J. C., Chapman, E. G., Grell, G. A., and Peckham, S. E.: Evolution of ozone, particulates, and aerosol direct radiative forcing in the vicinity of Houston using a fully coupled meteorology-chemistry-aerosol

Development and impact of hooks of high droplet concentration

R. C. George et al.

Title Page

Abstract

Introduction

Conclusions

References

Tables

Figures

⏪

⏩

◀

▶

Back

Close

Full Screen / Esc

Printer-friendly Version

Interactive Discussion

model, *J. Geophys. Res.-Atmos.*, 111, D21305, doi:10.1029/2005JD006721, 2006. 2501, 2502

George, R. C. and Wood, R.: Subseasonal variability of low cloud radiative properties over the southeast Pacific Ocean, *Atmos. Chem. Phys.*, 10, 4047–4063, doi:10.5194/acp-10-4047-2010, 2010. 2496, 2497, 2509

Gettelman, A., Liu, X., Ghan, S. J., Morrison, H., Park, S., Conley, A. J., Klein, S. A., Boyle, J., Mitchell, D. L., and Li, J. L. F.: Global simulations of ice nucleation and ice supersaturation with an improved cloud scheme in the community atmosphere model, *J. Geophys. Res.-Atmos.*, 115, D18216, doi:10.1029/2009JD013797, 2010. 2503

Gong, S. L., Barrie, L. A., and Blanchet, J. P.: Modeling sea-salt aerosols in the atmosphere 1. Model development, *J. Geophys. Res.-Atmos.*, 102, 3805–3818, doi:10.1029/96jd02953, 1997. 2501

Grell, G. A., Peckham, S. E., Schmitz, R., McKeen, S. A., Frost, G., Skamarock, W. C., and Eder, B.: Fully coupled “online” chemistry within the WRF model, *Atmos. Environ.*, 39, 6957–6975, doi:10.1016/j.atmosenv.2005.04.027, 2005. 2501

Gustafson Jr., W. I., Chapman, E. G., Ghan, S. J., Easter, R. C., and Fast, J. D.: Impact on modeled cloud characteristics due to simplified treatment of uniform cloud condensation nuclei during NEAQS 2004, *Geophys. Res. Lett.*, 34, L19809, doi:10.1029/2007GL030021, 2007. 2502

Huneus, N., Gallardo, L., and Rutllant, J. A.: Offshore transport episodes of anthropogenic sulfur in northern Chile: potential impact on the stratocumulus cloud deck, *Geophys. Res. Lett.*, 33, L19819, doi:10.1029/2006GL026921, 2006. 2495, 2497

Klein, S. A. and Hartmann, D. L.: The seasonal cycle of low stratiform clouds, *J. Climate*, 6, 1587–1606, doi:10.1175/1520-0442(1993)006<1587:TSCOLS>2.0.CO;2, 1993. 2496

Lohmann, U. and Feichter, J.: Global indirect aerosol effects: a review, *Atmos. Chem. Phys.*, 5, 715–737, doi:10.5194/acp-5-715-2005, 2005. 2495

Mena-Carrasco, M., Ruiz, P., Stambuk, A., Stambuk, L., Granifo, R., and Jerardino, M.: Antecedentes para la Revision de las Normas Primarias de Calidad de Aire para Dioxido de Azufre, Monoxido de Carbono, Ozono, Dioxido de Nitrogeno, Santiago, Chile, 2010. 2501

Morrison, H. and Pinto, J. O.: Mesoscale modeling of springtime Arctic mixed-phase stratiform clouds using a new two-moment bulk microphysics scheme, *J. Atmos. Sci.*, 62, 3683–3704, doi:10.1175/JAS3564.1, 2005. 2503

Development and impact of hooks of high droplet concentration

R. C. George et al.

Title Page

Abstract

Introduction

Conclusions

References

Tables

Figures

⏪

⏩

◀

▶

Back

Close

Full Screen / Esc

Printer-friendly Version

Interactive Discussion



Muñoz, R. C. and Alcañaz, R. I.: Variability of urban aerosols over Santiago, Chile: comparison of surface PM₁₀ concentrations and remote sensing with ceilometer and lidar, *Aerosol Air Qual. Res.*, 12, 8–19, doi:10.4209/aaqr.2011.08.0133, 2012. 2496

Nightingale, P. D., Malin, G., Law, C. S., Watson, A. J., Liss, P. S., Liddicoat, M. I., Boutin, J., and Upstill-Goddard, R. C.: In situ evaluation of air-sea gas exchange parameterizations using novel conservative and volatile tracers, *Global Biogeochem. Cy.*, 14, 373–387, doi:10.1029/1999GB900091, 2000. 2502

Painemal, D., Minnis, P., Ayers, J. K., and O'Neill, L.: GOES-10 microphysical retrievals in marine warm clouds: multi-instrument validation and daytime cycle over the southeast Pacific, *J. Geophys. Res.-Atmos.*, 117, D19212, doi:10.1029/2012JD017822, 2012. 2499

Penner, J. E., Andreae, M., Annegarn, H., Barrie, L., Feichter, J., Hegg, D., Jayaraman, A., Leaitch, R., Murphy, D., Nganga, J., and Pitari, G.: Aerosols, their direct and indirect effects, in: *Climate Change 2001: The Scientific Basis. Report to Intergovernmental Panel on Climate Change from the Scientific Assessment Working Group (WGI)*, edited by: Houghton, J. T., Ding, Y., Griggs, D. J., Noguer, M., Van der Linden, P. J., Dai, X., Maskell, K., and Johnson, C. A., Cambridge University Press, Cambridge, UK, 289–416, 2001. 2495

Platnick, S. and Twomey, S.: Determining the susceptibility of cloud albedo to changes in droplet concentrations with the advanced very high resolution radiometer, *J. Appl. Meteorol.*, 33, 334–347, doi:10.1175/1520-0450(1994)033<0334:DTSOCA>2.0.CO;2, 1994. 2495

Rahn, D. A. and Garreaud, R.: Marine boundary layer over the subtropical southeast Pacific during VOCALS-REx – Part 1: Mean structure and diurnal cycle, *Atmos. Chem. Phys.*, 10, 4491–4506, doi:10.5194/acp-10-4491-2010, 2010a. 2511, 2521

Rahn, D. A. and Garreaud, R.: Marine boundary layer over the subtropical southeast Pacific during VOCALS-REx – Part 2: Synoptic variability, *Atmos. Chem. Phys.*, 10, 4507–4519, doi:10.5194/acp-10-4507-2010, 2010b. 2496

Randall, D., Wood, R., Bony, S., Colman, R., Fichet, T., Fyfe, J., Kattsov, V., Pitman, A., Shukla, J., Srinivasan, J., Stouffer, R., Sumi, A., and Taylor, K.: Climate models and their evaluation, in: *Climate Change 2007: The Physical Science Basis. Contribution of Working Group I to the Fourth Assessment Report of the Intergovernmental Panel on Climate Change*, Cambridge University Press, Cambridge, UK and New York, NY, USA, 153–185, 2007. 2495

Riddle, E. E., Voss, P. B., Stohl, A., Holcomb, D., Maczka, D., Washburn, K., and Talbot, R. W.: Trajectory model validation using newly developed altitude-controlled balloons during the

Development and impact of hooks of high droplet concentration

R. C. George et al.

Title Page

Abstract

Introduction

Conclusions

References

Tables

Figures

⏪

⏩

◀

▶

Back

Close

Full Screen / Esc

Printer-friendly Version

Interactive Discussion

- International Consortium for Atmospheric Research on Transport and Transformations 2004 campaign, *J. Geophys. Res.-Atmos.*, 111, D23S57, doi:10.1029/2006JD007456, 2006. 2523
- Saide, P. E., Spak, S. N., Carmichael, G. R., Mena-Carrasco, M. A., Yang, Q., Howell, S., Leon, D. C., Snider, J. R., Bandy, A. R., Collett, J. L., Benedict, K. B., de Szoeke, S. P., Hawkins, L. N., Allen, G., Crawford, I., Crosier, J., and Springston, S. R.: Evaluating WRF-Chem aerosol indirect effects in Southeast Pacific marine stratocumulus during VOCALS-REx, *Atmos. Chem. Phys.*, 12, 3045–3064, doi:10.5194/acp-12-3045-2012, 2012. 2503
- Schell, B., Ackermann, I. J., Hass, H., Binkowski, F. S., and Ebel, A.: Modeling the formation of secondary organic aerosol within a comprehensive air quality model system, *J. Geophys. Res.-Atmos.*, 106, 28275–28293, doi:10.1029/2001JD000384, 2001. 2502
- Schüller, M., Estrada, A., and Bringezu, S.: Mapping environmental performance of international raw material production flows: a comparative case study for the copper industry of Chile and Germany, *Miner. Energ.*, 23, 29–45, 2008. 2496
- Schwartz, S. E., Harshvardhan, and Benkovitz, C. M.: Influence of anthropogenic aerosol on cloud optical depth and albedo shown by satellite measurements and chemical transport modeling, *P. Natl. Acad. Sci. USA*, 99, 1784–1789, doi:10.1073/pnas.261712099, 2002. 2495
- Seinfeld, J. and Pandis, S.: *Atmospheric Chemistry and Physics: From Air Pollution to Climate Change*, 1st edn., J. Wiley, New York, 1998. 2496
- Shank, L. M., Howell, S., Clarke, A. D., Freitag, S., Brekhovskikh, V., Kapustin, V., McNaughton, C., Campos, T., and Wood, R.: Organic matter and non-refractory aerosol over the remote Southeast Pacific: oceanic and combustion sources, *Atmos. Chem. Phys.*, 12, 557–576, doi:10.5194/acp-12-557-2012, 2012. 2502
- Snider, J. R., Petters, M. D., Wechsler, P., and Liu, P. S. K.: Supersaturation in the Wyoming CCN instrument, *J. Atmos. Ocean. Tech.*, 23, 1323–1339, doi:10.1175/JTECH1916.1, 2006. 2498
- Stockwell, W. R., Middleton, P., Chang, J. S., and Tang, X. Y.: The second generation regional acid deposition model chemical mechanism for regional air quality modeling, *J. Geophys. Res.-Atmos.*, 95, 16343–16367, doi:10.1029/JD095iD10p16343, 1990. 2502
- Stohl, A., Wotawa, G., Seibert, P., and Krompkolb, H.: Interpolation errors in wind fields as a function of spatial and temporal resolution and their impact on different types of kinematic trajectories, *J. Appl. Meteorol.*, 34, 2149–2165, doi:10.1175/1520-0450(1995)034<2149:IEIWFA>2.0.CO;2, 1995. 2523

Development and impact of hooks of high droplet concentration

R. C. George et al.

Title Page

Abstract

Introduction

Conclusions

References

Tables

Figures

⏪

⏩

◀

▶

Back

Close

Full Screen / Esc

Printer-friendly Version

Interactive Discussion

- Thornton, D. C., Bandy, A. R., Tu, F. H., Blomquist, B. W., Mitchell, G. M., Nadler, W., and Lenschow, D. H.: Fast airborne sulfur dioxide measurements by Atmospheric Pressure Ionization Mass Spectrometry (APIMS), *J. Geophys. Res.-Atmos.*, 107, 4632, doi:10.1029/2002JD002289, 2002. 2498
- 5 Toniazzo, T., Abel, S. J., Wood, R., Mechoso, C. R., Allen, G., and Shaffrey, L. C.: Large-scale and synoptic meteorology in the south-east Pacific during the observations campaign VOCALS-REx in austral Spring 2008, *Atmos. Chem. Phys.*, 11, 4977–5009, doi:10.5194/acp-11-4977-2011, 2011. 2496, 2511
- Tsapakis, M., Lagoudaki, E., Stephanou, E. G., Kavouras, I. G., Koutrakis, P., Oyola, P., and von Baer, D.: The composition and sources of PM_{2.5} organic aerosol in two urban areas of Chile, *Atmos. Environ.*, 36, 3851–3863, doi:10.1016/S1352-2310(02)00269-8, 2002. 2496
- 10 Twohy, C. H., Anderson, J. R., Toohey, D. W., Andrejczuk, M., Adams, A., Lytle, M., George, R. C., Wood, R., Saide, P., Spak, S., Zuidema, P., and Leon, D.: Impacts of aerosol particles on the microphysical and radiative properties of stratocumulus clouds over the Southeast Pacific ocean, *Atmos. Chem. Phys. Discuss.*, 12, 19715–19767, doi:10.5194/acpd-12-19715-2012, 2012. 2511
- 15 Twomey, S.: Pollution and planetary albedo, *Atmos. Environ.*, 8, 1251–1256, doi:10.1016/0004-6981(74)90004-3, 1974. 2495
- Wood, R.: Cancellation of aerosol indirect effects in marine stratocumulus through cloud thinning, *J. Atmos. Sci.*, 64, 2657–2669, doi:10.1175/JAS3942.1, 2007. 2495
- 20 Wood, R., Bretherton, C. S., Leon, D., Clarke, A. D., Zuidema, P., Allen, G., and Coe, H.: An aircraft case study of the spatial transition from closed to open mesoscale cellular convection over the Southeast Pacific, *Atmos. Chem. Phys.*, 11, 2341–2370, doi:10.5194/acp-11-2341-2011, 2011a. 2498
- 25 Wood, R., Mechoso, C. R., Bretherton, C. S., Weller, R. A., Huebert, B., Straneo, F., Albrecht, B. A., Coe, H., Allen, G., Vaughan, G., Daum, P., Fairall, C., Chand, D., Gallardo Klenner, L., Garreaud, R., Grados, C., Covert, D. S., Bates, T. S., Krejci, R., Russell, L. M., de Szoeke, S., Brewer, A., Yuter, S. E., Springston, S. R., Chaigneau, A., Toniazzo, T., Minnis, P., Palikonda, R., Abel, S. J., Brown, W. O. J., Williams, S., Fochesatto, J., Brioude, J., and Bower, K. N.: The VAMOS Ocean-Cloud-Atmosphere-Land Study Regional Experiment (VOCALS-REx): goals, platforms, and field operations, *Atmos. Chem. Phys.*, 11, 627–654, doi:10.5194/acp-11-627-2011, 2011b. 2497, 2500
- 30

Woodhouse, M. T., Carslaw, K. S., Mann, G. W., Vallina, S. M., Vogt, M., Halloran, P. R., and Boucher, O.: Low sensitivity of cloud condensation nuclei to changes in the sea-air flux of dimethyl-sulphide, *Atmos. Chem. Phys.*, 10, 7545–7559, doi:10.5194/acp-10-7545-2010, 2010. 2507

- 5 Yang, Q., W. I. Gustafson Jr., Fast, J. D., Wang, H., Easter, R. C., Morrison, H., Lee, Y.-N., Chapman, E. G., Spak, S. N., and Mena-Carrasco, M. A.: Assessing regional scale predictions of aerosols, marine stratocumulus, and their interactions during VOCALS-REx using WRF-Chem, *Atmos. Chem. Phys.*, 11, 11951–11975, doi:10.5194/acp-11-11951-2011, 2011. 2503

ACPD

13, 2493–2547, 2013

Development and impact of hooks of high droplet concentration

R. C. George et al.

Title Page

Abstract

Introduction

Conclusions

References

Tables

Figures

⏪

⏩

◀

▶

Back

Close

Full Screen / Esc

Printer-friendly Version

Interactive Discussion



Development and impact of hooks of high droplet concentration

R. C. George et al.

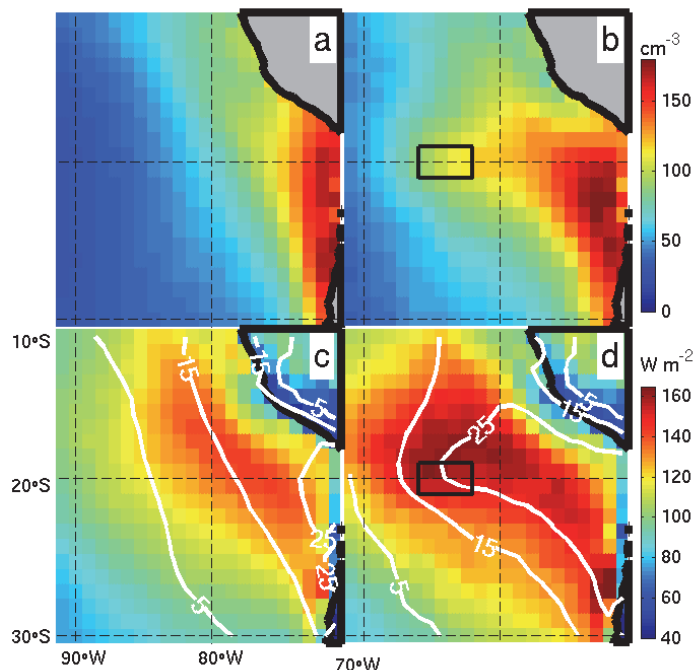


Fig. 1. 2000–2008 MODIS time-mean cloud droplet concentration (N_d) from **(a)** all retrieved days and **(b)** days when N_d averaged over the domain $19\text{--}21^\circ\text{S}$, $82\text{--}86^\circ\text{W}$ is larger than 87 cm^{-3} (time mean plus standard deviation). Shaded colors in **(c)** show the diurnal mean estimate of reflected solar flux at the top of the atmosphere. The white contour lines are the time mean of the difference between the reflected solar flux and the same flux computed using the typical pristine marine N_d (average time series of N_d in the domain $30\text{--}40^\circ\text{S}$, $90\text{--}100^\circ\text{W}$), which is an estimate of the Twomey effect. The contour numbers indicate W m^{-2} of flux difference due to the increase in N_d above typical marine values. **(d)** Is the same as **(c)**, but composite on the same days as **(b)**.

[Title Page](#)
[Abstract](#)
[Introduction](#)
[Conclusions](#)
[References](#)
[Tables](#)
[Figures](#)
[◀](#)
[▶](#)
[◀](#)
[▶](#)
[Back](#)
[Close](#)
[Full Screen / Esc](#)
[Printer-friendly Version](#)
[Interactive Discussion](#)

**Development and
impact of hooks of
high droplet
concentration**

R. C. George et al.

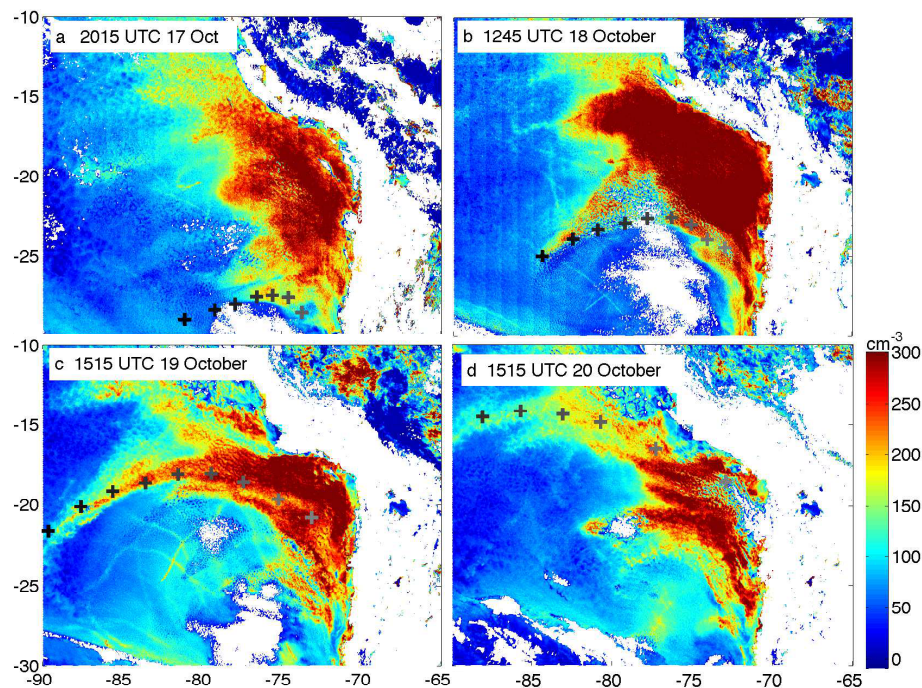


Fig. 2. Observations of Hook1 N_d derived from GOES retrievals (Sect. 2.1) on **(a)** 17 October at 20:15 UTC, **(b)** 18 October at 12:45 UTC, **(c)** 19 October at 15:15 UTC, and **(d)** 20 October at 15:15 UTC. Markers (“+”) show points along ECMWF MBL 2-D (at 950 hPa) forward and backward trajectories (see Appendix) initialized at locations along the hook on 18 October at 12:00 UTC.

Title Page

Abstract

Introduction

Conclusions

References

Tables

Figures

◀

▶

◀

▶

Back

Close

Full Screen / Esc

Printer-friendly Version

Interactive Discussion

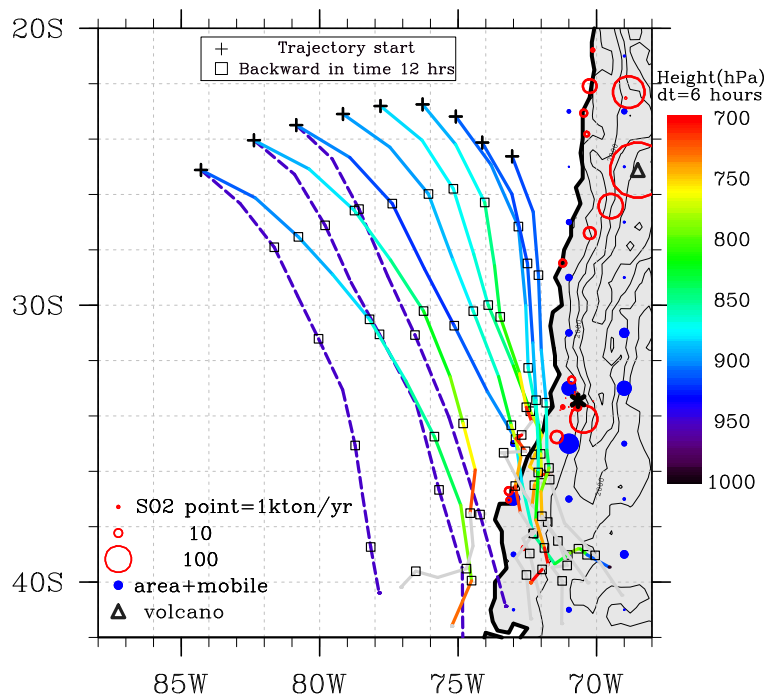


Fig. 3. ECMWF 3-D back trajectories initialized from 2-D hook MBL trajectory points on 18 October at 12:00 UTC (Fig. 2), but at the inversion level (the ECMWF level at which temperature is a minimum for relative humidity larger than 50 %) rather than 950 hPa. Colors represent trajectory heights in hPa, gray indicating heights above 700 hPa. Squares mark 12 h time intervals. Dashed lines show a few 950 hPa MBL 2-D trajectories from Fig. 2. Land contours are elevation height in 1000 m resolution and the “*” marks Santiago. SO₂ emissions from anthropogenic and volcanic sources are shown with open red circles for point sources (including smelters and volcanos) and blue filled circles demonstrating 2° × 2° average area + mobile urban and industrial sources.

Development and impact of hooks of high droplet concentration

R. C. George et al.

Title Page

Abstract Introduction

Conclusions References

Tables Figures

◀ ▶

◀ ▶

Back Close

Full Screen / Esc

Printer-friendly Version

Interactive Discussion



**Development and
impact of hooks of
high droplet
concentration**

R. C. George et al.

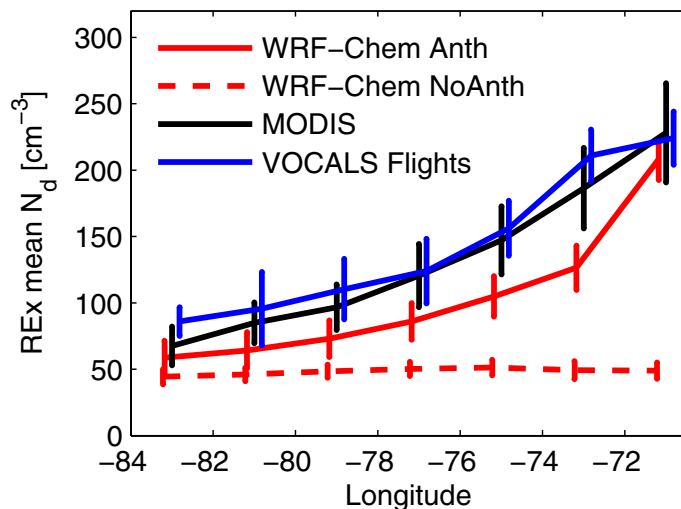


Fig. 4. VOCALS-REx mean N_d 19–21° S from MODIS retrievals (black), VOCALS flight data (blue) and WRF-Chem model output (red; at 15:00 UTC to compare with MODIS) for Anth (solid) and NoAnth (dashed) simulations in 2 degree longitude bins. Error bars show the 95% confidence interval of the standard error of the mean.

[Title Page](#)[Abstract](#)[Introduction](#)[Conclusions](#)[References](#)[Tables](#)[Figures](#)[◀](#)[▶](#)[◀](#)[▶](#)[Back](#)[Close](#)[Full Screen / Esc](#)[Printer-friendly Version](#)[Interactive Discussion](#)

**Development and
impact of hooks of
high droplet
concentration**

R. C. George et al.

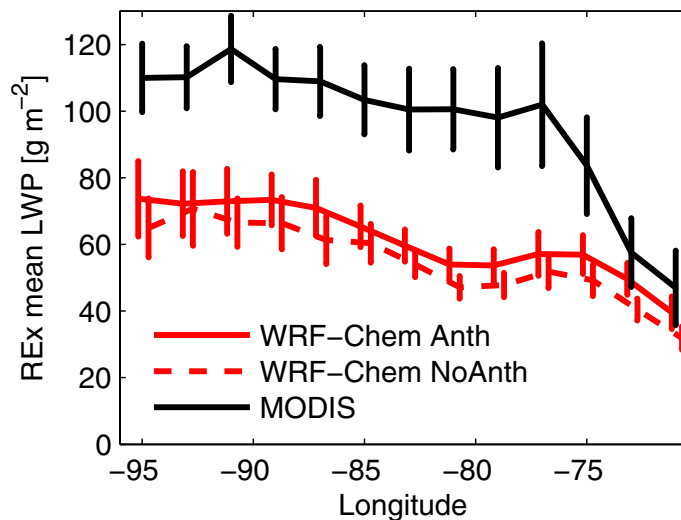


Fig. 5. VOCALS-REx mean LWP 19–21° S from MODIS (black) and WRF-Chem simulation at 15:00 UTC (red) for Anth (solid) and NoAnth (dashed) simulations in 2 degree longitude bins. Error bars show the 95 % confidence interval of the standard error of the mean.

[Title Page](#)[Abstract](#)[Introduction](#)[Conclusions](#)[References](#)[Tables](#)[Figures](#)[◀](#)[▶](#)[◀](#)[▶](#)[Back](#)[Close](#)[Full Screen / Esc](#)[Printer-friendly Version](#)[Interactive Discussion](#)

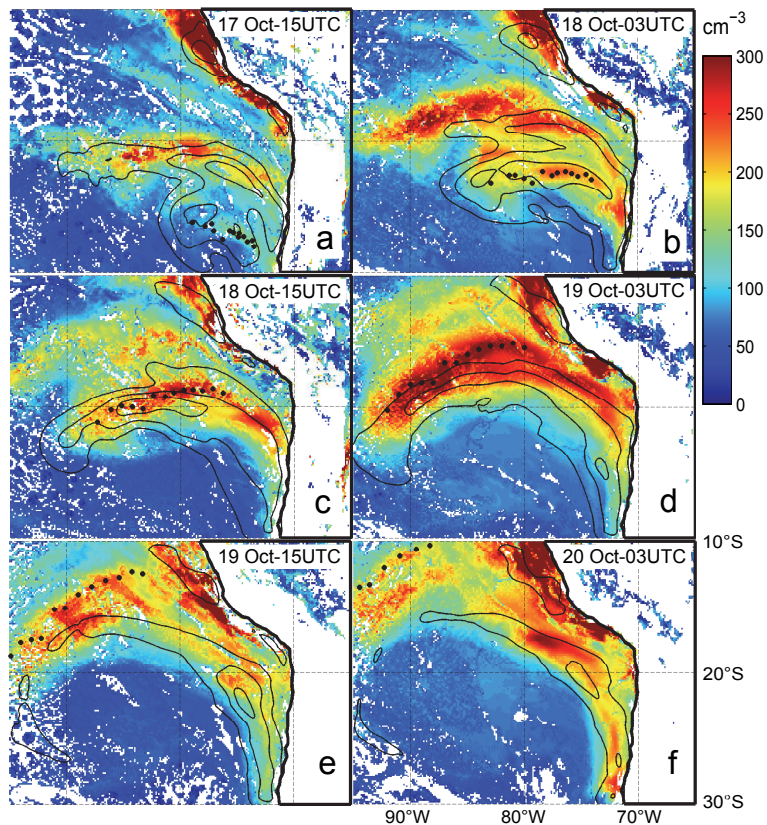


Fig. 6. Model N_d (colors) with filled black circle markers following thirteen WRF-Chem 2-D MBL trajectories. Trajectories are initialized from points along the peak N_d on 19 October at 03:00 UTC (d) 2 model levels below the inversion ($\sim 910\text{--}950$ hPa). They are computed forward until they reaches the NW corner of the domain, and backwards until 17 October at 03:00 UTC. Black contours are CCN in the model layer above the inversion at 100, 300 and 500 cm^{-3} .

Development and impact of hooks of high droplet concentration

R. C. George et al.

Title Page

Abstract Introduction

Conclusions References

Tables Figures

◀ ▶

◀ ▶

Back Close

Full Screen / Esc

Printer-friendly Version

Interactive Discussion



Development and impact of hooks of high droplet concentration

R. C. George et al.

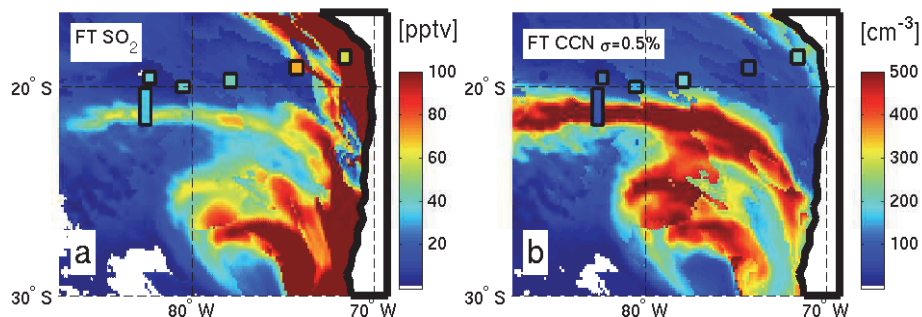


Fig. 7. Contours of model **(a)** SO_2 and **(b)** CCN at $\sigma = 0.5\%$ in the model level above the inversion on 17 October at 15:00 UTC, 24 h before the VOCALS C-130 RF02 flight (13:00–21:00 UTC 18 October) to correct for model and satellite observations time offset of N_d (Figs. 2 and 6). Superimposed rectangles show above-cloud flight leg mean data SO_2 measurements and CCN when measured for $\sigma = 0.4\text{--}0.5\%$.

[Title Page](#)
[Abstract](#)
[Introduction](#)
[Conclusions](#)
[References](#)
[Tables](#)
[Figures](#)
[⏪](#)
[⏩](#)
[◀](#)
[▶](#)
[Back](#)
[Close](#)
[Full Screen / Esc](#)
[Printer-friendly Version](#)
[Interactive Discussion](#)

Development and impact of hooks of high droplet concentration

R. C. George et al.

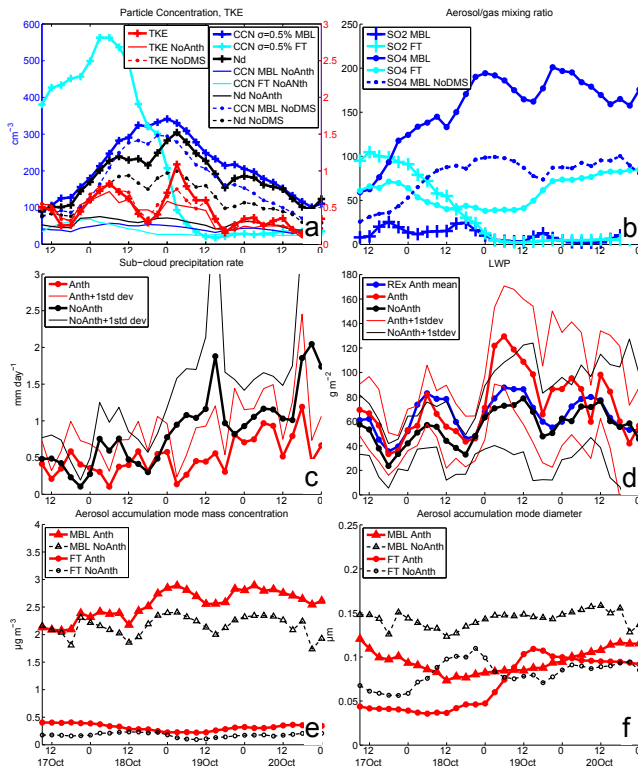


Fig. 8. Average of cloud and aerosol properties interpolated along ninety-five 2-D hook trajectories, computed in the same manner as those marked Fig. 6, both in the model layer just above the inversion (FT) and in the MBL at the cloud level. **(a)** FT CCN (cyan) and MBL CCN (blue) at 0.5% SS with N_d (black) and turbulent kinetic energy (red). The Anth simulation has “+” markers. Lines without markers are the NoAnth simulation and circle markers with dashed lines indicate the NoDMS simulation. **(b)** SO_2 (“+”) and SO_4 (circles) in the FT (cyan) and MBL (blue). The dashed blue line indicates NoDMS MBL SO_4 . In **(c–f)** properties in the Anth (red) and NoAnth (black) are compared. Thin solid lines indicate 1 standard deviation outside the mean of hook points. **(c)** Precipitation rate simulations at sub-cloud level. **(d)** LWP and REx mean LWP at the same time of day at hook trajectory locations (blue). Accumulation mode aerosol mass and computed accumulation mode diameters are shown in the **(e)** and **(f)** in the MBL (triangles) and FT (circles).

Title Page

Abstract Introduction

Conclusions References

Tables Figures

◀ ▶

◀ ▶

Back Close

Full Screen / Esc

Printer-friendly Version

Interactive Discussion

Development and impact of hooks of high droplet concentration

R. C. George et al.

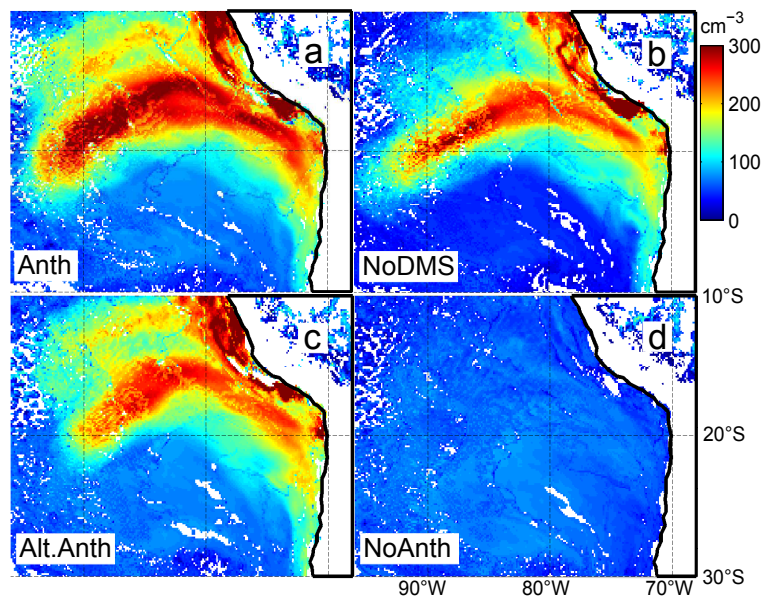


Fig. 9. Snapshots of N_d on 19 October at 03:00 UTC from different simulations: **(a)** Anth, full anthropogenic emissions, includes DMS; **(b)** NoDMS, full anthropogenic emissions, no DMS; **(c)** Alternative Anth: no anthropogenic emissions south of 30° S, east of 70° W, includes DMS; **(d)** NoAnth, no anthropogenic emissions, includes DMS.

[Title Page](#)[Abstract](#)[Introduction](#)[Conclusions](#)[References](#)[Tables](#)[Figures](#)[⏪](#)[⏩](#)[◀](#)[▶](#)[Back](#)[Close](#)[Full Screen / Esc](#)[Printer-friendly Version](#)[Interactive Discussion](#)

Development and impact of hooks of high droplet concentration

R. C. George et al.

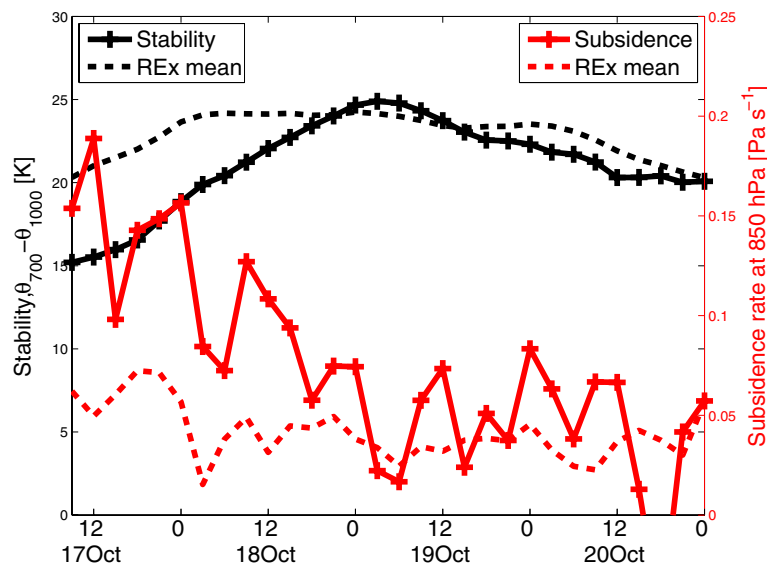


Fig. 10. Average stability (black) and 850 hPa subsidence rate (red) interpolated over Hook1 2-D trajectories (same trajectories used in Fig. 8). Stability is defined as the difference in potential temperature between 700 hPa and 1000 hPa ($\theta_{700} - \theta_{1000}$) and subsidence is the grid-scale vertical velocity in pressure units (Pa s^{-1}). Crosses mark the Anth simulation and dashed lines denote the REx mean at the locations and times of day of the Hook1 trajectories.

[Title Page](#)
[Abstract](#)
[Introduction](#)
[Conclusions](#)
[References](#)
[Tables](#)
[Figures](#)
[⏪](#)
[⏩](#)
[◀](#)
[▶](#)
[Back](#)
[Close](#)
[Full Screen / Esc](#)
[Printer-friendly Version](#)
[Interactive Discussion](#)

Development and impact of hooks of high droplet concentration

R. C. George et al.

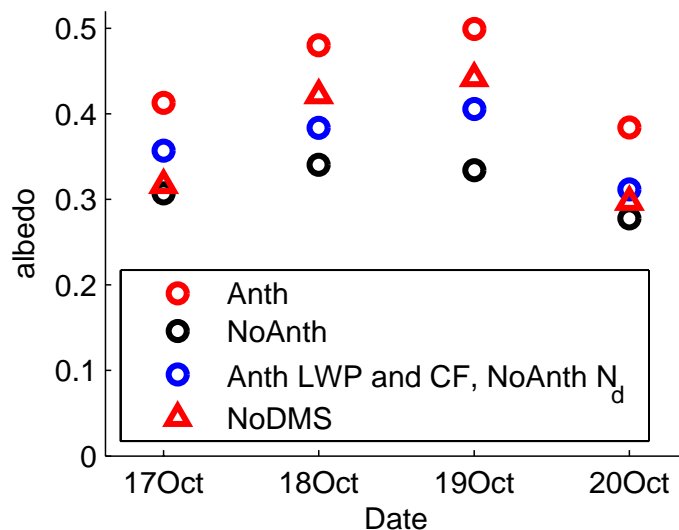


Fig. 11. Average albedo interpolated over Hook1 2-D trajectories (same trajectories used in Fig. 8) and averaged over each day, weighted by solar insolation. The Anth (red circles), NoAnth (black), and NoDMS (red triangles) simulations are shown. The blue circles are albedo computed using Anth LWP and CF, and NoAnth N_d and include a correction for biases caused by WRF-Chem's binary CF (average the Twomey effect estimates using Anth and NoAnth as the base simulations with constant LWP and CF). The Twomey effect estimate is thus the difference between red and blue circles, while secondary effects are represented by the difference between blue and black circles.

[Title Page](#)[Abstract](#) [Introduction](#)[Conclusions](#) [References](#)[Tables](#) [Figures](#)[◀](#) [▶](#)[◀](#) [▶](#)[Back](#) [Close](#)[Full Screen / Esc](#)[Printer-friendly Version](#)[Interactive Discussion](#)

Development and impact of hooks of high droplet concentration

R. C. George et al.

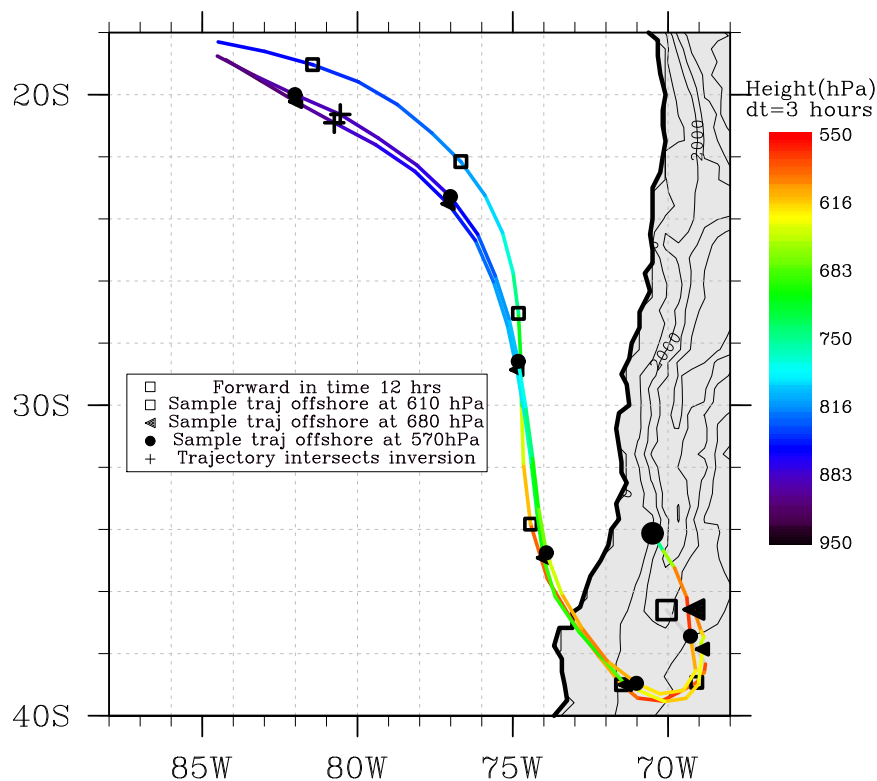


Fig. 12. Three forward WRF-Chem trajectories from 15 October at 18:00 UTC to 19 October at 00:00 UTC that follow polluted CCN in the FT from land to Hook1 and advect offshore at different heights. Markers indicate 12 h intervals and marker shapes distinguish the trajectories. Circle markers follow the trajectory shown in Figs. 13 and 14.

Title Page

Abstract

Introduction

Conclusions

References

Tables

Figures

◀

▶

◀

▶

Back

Close

Full Screen / Esc

Printer-friendly Version

Interactive Discussion

Development and impact of hooks of high droplet concentration

R. C. George et al.

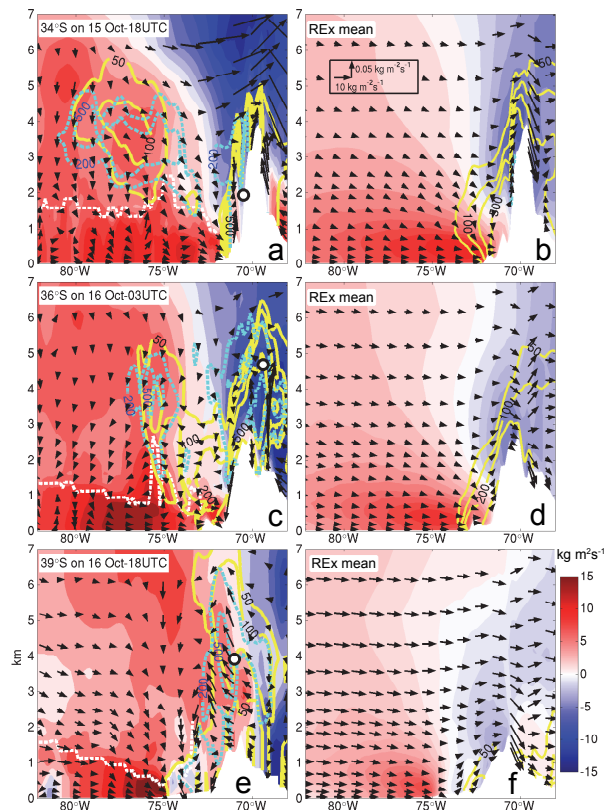


Fig. 13. WRF-Chem zonal transects at latitudes following a WRF-Chem 3-D trajectory (white circle markers here, following the trajectory marked with circle in Fig. 12) of winds (multiplied by density to give mass fluxes), CCN at 0.5% supersaturation (cyan dashed lines) at 200 and 500 cm^{-3} (labeled blue), and SO_2 concentrations (yellow lines) at 50, 100, 200 and 500 ppptv (labeled black). Filled colored contours show the magnitude of the meridional component of wind (positive is southerly flow), while vectors show zonal and vertical components. The white dashed line indicates an estimate of the inversion height. Left columns are interpolated snapshots at the time of the trajectory and right columns show REEx mean properties at the same latitude.

Development and impact of hooks of high droplet concentration

R. C. George et al.

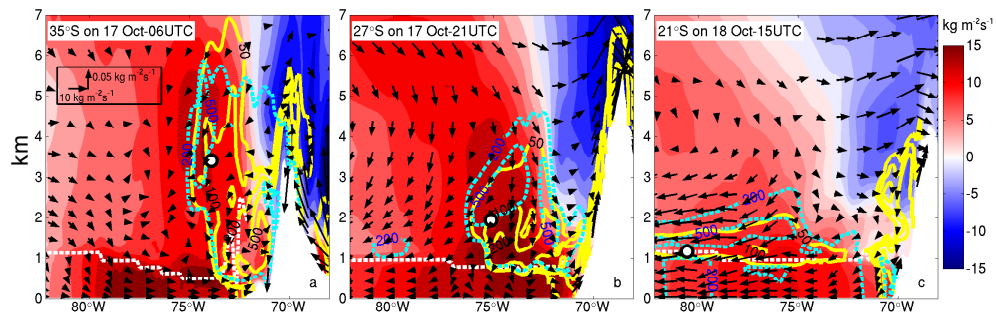


Fig. 14. Same as left column of Fig. 13, but for second half of the WRF-Chem 3-D trajectory (circle markers in Fig. 12) described in Sect. 4.4 as it advects northwest and subsides towards the boundary layer.

Title Page

Abstract

Introduction

Conclusions

References

Tables

Figures

◀

▶

◀

▶

Back

Close

Full Screen / Esc

Printer-friendly Version

Interactive Discussion

Development and impact of hooks of high droplet concentration

R. C. George et al.

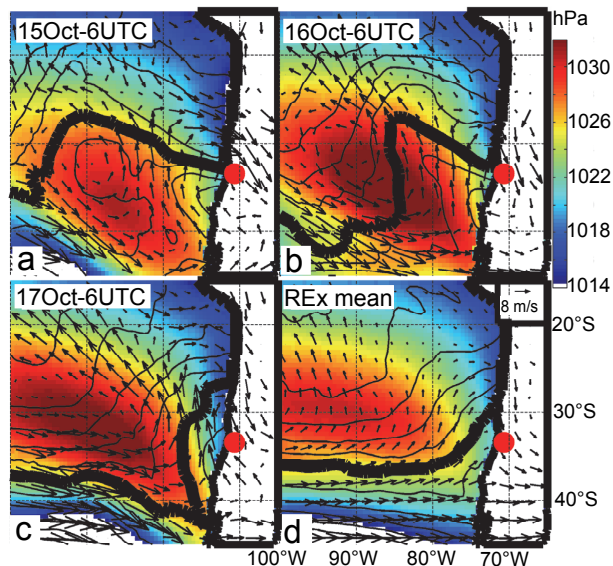


Fig. 15. WRF-Chem simulation surface pressure (colored contours), 500 hPa heights (line contours) and 700 hPa winds (arrows) at **(a–c)** in days preceding Hook1 at 06:00 UTC, and **(d)** REX mean conditions. The red circle marks Santiago. The bold 500 hPa contour is 5350 m and the contour interval is 50 m.

[Title Page](#)
[Abstract](#)
[Introduction](#)
[Conclusions](#)
[References](#)
[Tables](#)
[Figures](#)
[◀](#)
[▶](#)
[◀](#)
[▶](#)
[Back](#)
[Close](#)
[Full Screen / Esc](#)
[Printer-friendly Version](#)
[Interactive Discussion](#)

Development and impact of hooks of high droplet concentration

R. C. George et al.

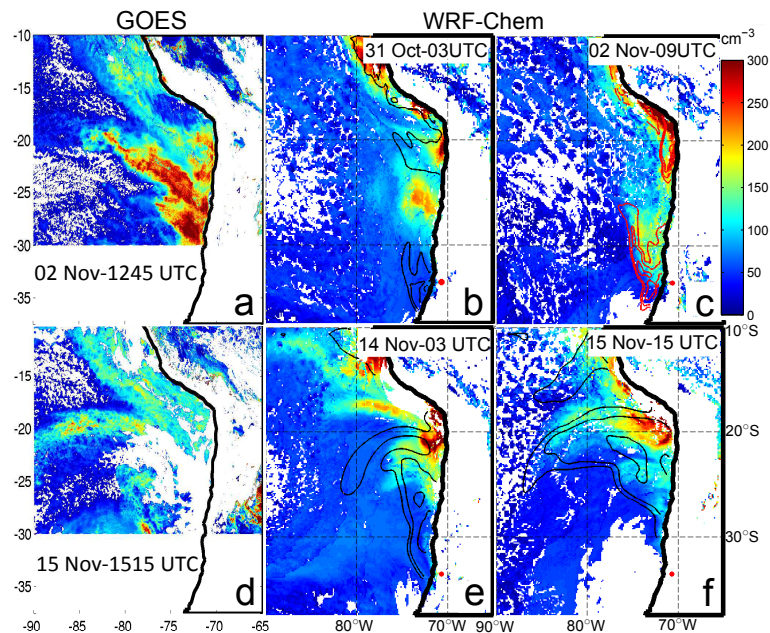


Fig. 16. GOES-derived N_d of Hook2 on 2 November at 12:45 UTC in **(a)** and of Hook3 on 15 November at 15:15 UTC in **(e)**, with model N_d snapshots on **(b)** 31 October at 03:00 UTC, **(c)** 2 November at 09:00 UTC (chosen because it demonstrates closer agreement with **(a)** than other times), **(e)** 14 November at 03:00 UTC and **(f)** 15 November at 15:00 UTC. The red dot marks Santiago. Black contours are FT maximum CCN at 0.5% at 100, 200 and 500 cm^{-3} . By **(c)** marine FT CCN is $<100 \text{ cm}^{-3}$ near the region of large N_d , so instead SO_2 at 100, 200, and 400 pptv is shown in red contours.

[Title Page](#)
[Abstract](#)
[Introduction](#)
[Conclusions](#)
[References](#)
[Tables](#)
[Figures](#)
[◀](#)
[▶](#)
[◀](#)
[▶](#)
[Back](#)
[Close](#)
[Full Screen / Esc](#)
[Printer-friendly Version](#)
[Interactive Discussion](#)

Development and impact of hooks of high droplet concentration

R. C. George et al.

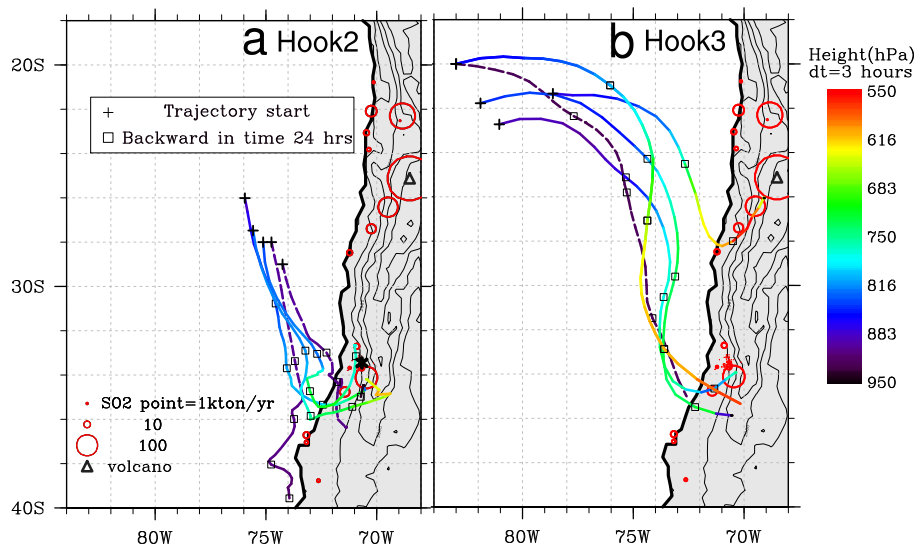


Fig. 17. WRF-Chem 3-D back trajectories (solid) initialized from points in the model level above the inversion within region of large SO_2 concentrations and 2-D back trajectories (dashed) in the MBL (2 model levels below the inversion) at points of large model N_d . Trajectories are initialized on **(a)** 2 November at 09:00 UTC corresponding to the model Hook2 in Fig. 16c and **(b)** 15 November at 15:00 UTC corresponding to the model Hook3 in Fig. 16f. Square markers indicate 24 h intervals and red circles are SO_2 point sources as in Fig. 3.

Title Page

Abstract

Introduction

Conclusions

References

Tables

Figures

◀

▶

◀

▶

Back

Close

Full Screen / Esc

Printer-friendly Version

Interactive Discussion